Iron and Manganese Alkoxide Cubes

Kingsley L. Taft,[1a] Andrea Caneschi,[1b] Laura E. Pence,[1a] Christopher D. Delfs,[1b] Georgia C. Papaefthymiou,[1c] and Stephen J. Lippard*,[1a]

Contribution from the Department of Chemistry and Francis Bitter National Magnet Laboratory, Massachusetts Institute of Technology, Cambridge, Massachusetts 02139, and Dipartimento di Chimica, Università degli Studi di Firenze, Italia, 50144

Received February 10, 1993®

Abstract: Four complexes with cubic $\{M_4(OR)_4\}^{n+}$ cores, $[Fe(OMe)(MeOH)(DPM)]_4$ (**1**), $[Fe(OMe)(MeOH)(DBM)]_4$ (**2**), $[Fe^{III}Fe^{II}_3(OMe)_5(MeOH)_3(OBz)_4]$ (**3**), and $[Mn_4(OEt)_4(EtOH)_2(DPM)_4]$ (**4**), have been prepared and crystallographically characterized. The four metal ions and bridging alkoxide ligands are located at alternating vertices of a cube, with either alcohol or alkoxide and β-diketonate or benzoate ligands on the exterior of the core. Complexes **1**, **2**, and **4** were synthesized in a single, high-yield step from MCl_2, the β-diketone, and 2 equiv of the appropriate lithium alkoxide, whereas **3** was isolated upon the slow oxidation by dioxygen of $FeCl_2$ in the presence of methoxide and benzoate. Complexes **1**, **2**, and **4** have all divalent metal ions, whereas cube **3** is a mixed-valent complex, with one iron(III) site. The terminal methanol coordinated to the ferric ion in **3** is deprotonated. The molecular symmetry ranges from S_4 for **1** and **2** to C_2 for **3** and C_1 for **4**. The iron atoms in **1–3** are octahedrally coordinated, whereas two of the four manganese ions in **4** have a distorted square pyramidal geometry. The cubes exhibit multiple electronic spectral features giving rise to the intense red, blue, green, and yellow colors of **1–4**, respectively. These absorptions have been assigned to metal–ligand charge-transfer transitions, spin-allowed d–d transitions, and, for mixed-valent **3**, an intervalence-charge-transfer band. The spectral studies in combination with ^1H NMR and solution Mössbauer experiments suggest that the cubes remain intact in solvent mixtures containing alcohol. Complexes **1** and **2** display a single quadrupole doublet in their high-temperature Mössbauer spectra with parameters characteristic of high-spin iron(II). The ferrous ions in **3** also produce a single quadrupole doublet, and the lone ferric ion is valence-localized, as revealed by both the structural study at −85 °C and its Mössbauer spectra, which display no delocalization up to 250 K. At low temperatures, polycrystalline samples of **2** and **3** exhibit magnetic hyperfine interactions in the absence of an applied field, whereas complex **1** does not. The solution spectrum of **2** at 4.2 K consists of a single quadrupole doublet, suggesting that the slow relaxation is a solid-state effect. Solution studies of **3** are less definitive, and for both **2** and **3**, the exact source of the increased relaxation times remains uncertain. The iron atoms in the $\{Fe_4(OMe)_4\}^{4+}$ cube **1** are ferromagnetically exchange-coupled, with a coupling constant $J = -1.88$ cm^{-1} ($H = J\sum_i^j \mathbf{S}_i \cdot \mathbf{S}_j$ where $j > i$), $g = 2.29$, and contributions from zero-field splitting. The predicted $S_T = 8$ ground state for **1** is confirmed by its saturation moment, which at 1.2 K is 15.7 μ_B in a 19.7 T field. The spin multiplet has significant anisotropy, with $D = 3$ cm^{-1}, $E/D = 0.075$, and $g = 2.2$. In contrast, the iron atoms of the mixed-valent $\{Fe_4(OMe)_4\}^{5+}$ core of **3** are antiferromagnetically exchange-coupled. Coupling constants of 2.60 and 1.63 cm^{-1} with a composite $g = 2.18$ were determined for the Fe(II)–Fe(II) and Fe(II)–Fe(III) exchange interactions, respectively. As evident from these results, the iron and manganese alkoxide cubes display a remarkable variety of structural, physical, and electronic properties; and the facile synthesis of **1–4** affords a convenient route to the $\{M_4(OR)_4\}^{n+}$ cubane architecture for iron and manganese.

Introduction

The arrangement of four metal ions and four bridging ligands at alternating corners of a cube is a well-precedented unit in inorganic chemistry. Among the most thoroughly studied members of this class are $\{Fe_4S_4\}^{n+}$ clusters, many of which were prepared and characterized as models for the active sites of iron–sulfur proteins.[2] More recently, following the proposal of a cubic arrangement of manganese ions and bridging ligands for the oxygen evolving center (OEC) of photosystem II,[3] several $\{Mn_4X_4\}^{n+}$ complexes with bridging oxo, chloro, or alkoxo ligands were synthesized as models for this postulated unit.[4-6] Cubic compounds containing the $\{Fe_4(OR)_4\}^{n+}$ core, however, are virtually unknown, although tetranuclear units with other geometries have been reported.[7] Included are a few iron(II) and mixed-valent iron complexes with bridging oxygen atoms,[8] and a larger number of tetrairon(III) species.[9] Tetranuclear $\{Fe^{III}_4(OR)_4\}^{8+}$ cubes have not yet been prepared, and only one tetrairon(II) analog, having bridging oxygen atoms derived from catecholate ligands, has been synthesized.[8a]

In the present article we describe a facile synthetic route to discrete tetranuclear iron and manganese alkoxide complexes $[Fe(OMe)(MeOH)(DPM)]_4$ (**1**), $[Fe(OMe)(MeOH)(DBM)]_4$ (**2**), $[Fe_4(OMe)_5(MeOH)_3(OBz)_4]$ (**3**), and $[Mn_4(OEt)_4(EtOH)_2(DPM)_4]$ (**4**).[10] The structures and physical properties of these molecules are also reported. Complexes **1**, **2**, and **4** contain four divalent metal ions, whereas **3** is a mixed-valent complex, with one iron(III) site. The $\{M_4(OR)_4\}^{n+}$ cores contain iron or manganese with triply bridging alkoxide ligands arranged at

® Abstract published in *Advance ACS Abstracts*, November 1, 1993.

(1) (a) Department of Chemistry, Massachusetts Institute of Technology. (b) Università degli Studi di Firenze. (c) Francis Bitter National Magnet Laboratory.

(2) (a) Berg, J. M.; Holm, R. H. In *Iron-Sulfur Proteins*; Spiro, T. G., Ed.; John Wiley & Sons: New York, 1982; Vol. 4, p. 1. (b) Holm, R. H.; Ciurli, S.; Weigel, J. A. *Prog. Inorg. Chem.* **1990**, *38*, 1.

(3) Brudvig, G. W.; Thorp, H. H.; Crabtree, R. H. *Acc. Chem. Res.* **1991**, *24*, 311.

(4) Wieghardt, K. *Angew. Chem., Int. Ed. Engl.* **1989**, *28*, 1153.

(5) Brooker, S.; McKee, V.; Shepard, W. B.; Pannell, L. K. *J. Chem. Soc. Dalton Trans.* **1987**, 2555.

(6) (a) Wemple, M. W.; Tsai, H.-L.; Folting, K.; Hendrickson, D. N.; Christou, G. *Inorg. Chem.* **1993**, *32*, 2025 and references therein. (b) Hendrickson, D. N.; Christou, G.; Schmitt, E. A.; Libby, E.; Bashkin, J. S.; Wang, S.; Tsai, H.-L.; Vincent, J. B.; Boyd, P. D. W.; Huffman, J. C.; Folting, K.; Li, Q.; Streib, W. E. *J. Am. Chem. Soc.* **1992**, *114*, 2455 and references therein.

(7) Review articles: (a) Lippard, S. J. *Angew. Chem., Int. Ed. Engl.* **1988**, *27*, 344. (b) Hagen, K. S. *Angew. Chem., Int. Ed. Engl.* **1992**, *31*, 1010.

(8) (a) Shoner, S. C.; Power, P. P. *Inorg. Chem.* **1992**, *31*, 1001. (b) Cotton, F. A.; Rice, G. W. *Nouv. J. Chim.* **1977**, *1*, 301. (c) Arena, F.; Floriani, C.; Chiesi-Villa, A.; Guastini, C. *J. Chem. Soc., Chem. Commun.* **1986**, 1369.

0002-7863/93/1515-11753$04.00/0

alternating vertices of a cube, the terminal positions of which are filled by either alcohol or alkoxide and β-diketonate or benzoate donor ligands. The preparation and characterization of **1–4** are significant additions to the class of polynuclear complexes of iron and manganese.

Experimental Section

Synthetic Procedures. The starting materials $FeCl_2$ and $MnCl_2$ were obtained from Strem, and HDPM, HDBM, HOBz, and a 1.6 M hexane solution of *n*-BuLi were purchased from Aldrich. All solvents were dried and distilled under a nitrogen atmosphere, except for C_6D_6, CD_3OD, and CD_2Cl_2, which were used as received after purging with Ar. All procedures were performed under the strict exclusion of air, unless otherwise noted.

[Fe(OMe)(MeOH)(DPM)]$_4$ (1). A slurry of 0.859 g (6.78 mmol) of $FeCl_2$ in 25 mL of MeOH was added to 1.250 g (6.78 mmol) of neat HDPM to give a light orange mixture. The LiOMe reagent (13.6 mmol, 2 equiv) was prepared by allowing 8.5 mL of a 1.6 M BuLi solution in hexane to react with 25 mL of MeOH. Addition of 1 equiv of this solution to the $FeCl_2$/HDPM reaction mixture turned it light yellow. A deep red precipitate formed immediately upon addition of the second equivalent. The [Fe(OMe)(MeOH)(DPM)]$_4$ product was collected by filtration and washed with excess MeOH, and the light yellow filtrate and washings were discarded. Large red parallelepiped crystals, the longest dimension of which measured >1 cm, were grown by layering 75 mL of MeOH over a 25-mL toluene solution of the red solid. In this manner, 1.689 g (82% yield) of **1** was isolated. Anal. Calcd for **1**, $C_{52}H_{104}O_{16}Fe_4$: C, 51.67; H, 8.67; Fe, 18.48. Found: C, 51.64; H, 8.20; Fe, 17.80. IR (KBr, cm^{-1}) 3424, 2961, 2915, 2869, 2812, 1568, 1536, 1501, 1455, 1387, 1356, 1223, 1182, 1140, 1036, 869, 791, 477. Electronic spectrum in 90% toluene/10% MeOH, λ_{max} (ϵ, M^{-1} cm^{-1}): 1125 (15), 810 (125), 540 (sh), 494 (2600), 359 (1500). ^1H NMR in 90% C_6D_6/10% CD_3OD δ, ppm (T_1, ms): 13.9 (3.6), 3.31 (7.1).

[Fe(OMe)(MeOH)(DBM)]$_4$·toluene, (2)·toluene. A procedure identical to that used to prepare **1** was employed. From the reaction in MeOH of 0.565 g (4.46 mmol) of $FeCl_2$, 1.000 g (4.46 mmol) of HDBM, and 5.6 mL of a 1.6 M BuLi solution in hexane (8.92 mmol, 2 equiv) was isolated a dark blue solid. Crystals of **2** were grown by layering MeOH on top of a saturated THF or toluene solution of the compound. From toluene/MeOH crystallizations, 1.254 g of **2**·toluene was obtained (77% yield). Anal. Calcd for **2**·toluene, $C_{75}H_{80}O_{16}Fe_4$: C, 61.67; H, 5.52. Found: C, 60.96; H, 5.60. IR (KBr, cm^{-1}) 3280, 2926, 2882, 2812, 1594, 1544, 1515, 1476, 1371, 1303, 1289, 1224, 1180, 1116, 1070, 1031, 931, 785, 758, 720, 691, 619, 521. Electronic spectrum in 90% toluene/10% MeOH, λ_{max} (ϵ, M^{-1} cm^{-1}): 780 (sh), 640 (5200), 575 (sh), 410 (sh). ^1H NMR in 90% C_6D_6/10% CD_3OD δ, ppm (T_1, ms): 18.6 (38), 16.8, 14.0 (3.2). Resonances attributable to the toluene of crystallization were also observed in the spectrum.

[Fe$_4$(OMe)$_5$(MeOH)$_3$(OBz)$_4$]·2MeOH, (3)·2MeOH. As described above, a clear, light orange methanol solution of 1.000 g (7.89 mmol) of $FeCl_2$, 0.963 g (7.89 mmol) of HOBz, and 9.9 mL of a 1.6 M BuLi hexane solution (15.8 mmol, 2 equiv) was prepared. A small amount of orange precipitate was removed by filtration. The solution was sealed in a single-neck flask with a rubber septum and stored over anhydrous calcium sulfate in a desiccator filled with air. The reaction solution turned deep green over several days as air diffused into the flask, after which time well-shaped rectangular blocks of [Fe$_4$(OMe)$_5$(MeOH)$_3$(OBz)$_4$]·2MeOH, **3**·2MeOH, had formed. Complex **3**·2MeOH was collected under an inert atmosphere, crushed to a powder, and dried under vacuum to give 0.390 g (21%) of desolvated **3**. Air could be added directly to the reaction solution to generate the green color, instead of the slower diffusion process, but this procedure precipitated a yellow powder in addition to **3**·2MeOH, which was obtained in lower yield. Anal. Calcd for **3**, $C_{36}H_{47}O_{16}Fe_4$: C, 45.08; H, 4.94; Fe, 23.29. Found: C, 44.88; H, 4.74; Fe, 22.95. IR (KBr, cm^{-1}) 3290, 2928, 2826, 1600, 1547, 1401, 1175, 1067, 1055, 1026, 835, 718, 688, 677, 574, 450. Electronic spectrum in 50% CH_2Cl_2/50% MeOH or their deuterated analogs, λ_{max} (ϵ, M^{-1} cm^{-1}): 925 (295), 705 (300), 353 (sh).

[Mn$_4$(OEt)$_4$(EtOH)$_2$(DPM)$_4$] (4). In a typical reaction, a solution of 0.100 g (0.795 mmol) of anhydrous $MnCl_2$ in 1 mL of EtOH was added to 0.146 g (0.795 mmol) of neat HDPM. In a separate flask, 1.0 mL of a 1.6 M solution of BuLi in hexane (1.59 mmol, 2 equiv) was added to 10 mL of EtOH to generate the LiOEt reagent. The latter solution was added to the manganese solution and agitated to ensure complete mixing. A bright yellow microcrystalline solid precipitated immediately and was collected in quantitative yield by vacuum filtration, leaving a colorless filtrate. The product was dissolved in toluene and filtered to remove any impurities, and the resulting solution was layered with EtOH to induce crystallization of the product. The final pure material was collected by filtration in 62% yield. Anal. Calcd for **4**, $C_{56}H_{108}O_{14}Mn_4$: C, 54.90; H, 8.88. Found: C, 54.84; H, 8.07. IR (KBr, cm^{-1}) 3351, 2964, 2883, 1584, 1542, 1503, 1456, 1413, 1359, 1277, 1222, 1182, 1133, 1094, 1041, 872, 793, 760, 738, 607, 479. Electronic spectrum in 90% CH_2Cl_2/10% EtOH, λ_{max} (ϵ, M^{-1} cm^{-1}): 301 (62,400).

X-ray Crystallography. Crystalline samples were mounted and data were collected at low temperatures under a flowing stream of dinitrogen. Data collection and reduction and other general procedures were as previously described.[11] A systematic search for the highest possible Laue symmetry using TRACER-II was conducted for each structure.[12] No appreciable decay was observed for any of the complexes. Initial metal positions were determined by using the direct methods program SHELXS-86.[13] The remaining heavy atoms were located from DIRDIF,[14] and the TEXSAN program package was used to refine the structures.[15] All non-hydrogen atoms were refined with anisotropic thermal parameters in the final cycles, except for the disordered atoms described below. Hydrogen atoms bound to carbon were calculated at a C–H distance of 0.95 Å, with hydrogen thermal parameters set equal to 1.2 × B_{eq} of the attached carbon atom. Absorption corrections based on ψ-scans for **1**, **3**, and **4** were applied.[16] Relevant crystallographic information is summarized in Table I. Final positional and thermal parameters and listings of interatomic distances and angles for **1–4** are supplied as supplementary material.

[Fe(OMe)(MeOH)(DPM)]$_4$ (1). A rectangular crystal with dimensions of 0.38 × 0.53 × 0.70 mm was cut from a larger crystal and mounted with hydrocarbon grease on the end of a quartz fiber. The crystal diffracted well, $\Delta\bar{\omega}_{1/2}$ for several low-angle reflections being 0.27°. From the Laue symmetry and systematic absences, the space group was determined to be $P2_1/n$. Because of the long *b*-axis, ω-scans were used for data collection. The largest shift/esd in the final cycle of refinement was 0.0003, and the largest peak in the final difference Fourier map contained 0.46 e/Å^3 near two DPM methyl groups.

[Fe(OMe)(MeOH)(DBM)]$_4$·toluene, (2)·toluene. A deep blue needle measuring 0.20 × 0.25 × 0.58 mm, grown by layering MeOH on a toluene solution of **2**, was attached to a quartz fiber with hydrocarbon grease.

(9) (a) Ponomarev, V. I.; Atovmyan, L. O.; Bobkova, S. A.; Turté, K. I. *Dokl. Akad. Nauk SSSR* **1984**, *274*, 368. (b) Stukan, R. A.; Ponomarev, V. I.; Nifontov, V. P.; Turté, K. I.; Atovmyan, L. O. *J. Struct. Chem.* **1985**, *26*, 197. (c) Toftlund, H.; Murray, K. S.; Zwack, P. R.; Taylor, L. F.; Anderson, O. P. *J. Chem. Soc., Chem. Commun.* **1986**, 191. (d) Jameson, D. L.; Xie, C.-L.; Hendrickson, D. N.; Potenza, J. A.; Schugar, H. J. *J. Am. Chem. Soc.* **1987**, *109*, 740. (e) Armstrong, W. H.; Roth, M. E.; Lippard, S. J. *J. Am. Chem. Soc.* **1987**, *109*, 6318. (f) Murch, B. P.; Bradley, F. C.; Boyle, P. D.; Papaefthymiou, V.; Que, L., Jr. *J. Am. Chem. Soc.* **1987**, *109*, 7993. (g) Gorun, S. M.; Lippard, S. J. *Inorg. Chem.* **1988**, *27*, 149. (h) Chen, Q.; Lynch, J. B.; Gomez-Romero, P.; Ben-Hussein, A.; Jameson, G. B.; O'Connor, C. J.; Que, L., Jr. *Inorg. Chem.* **1988**, *27*, 2673. (i) Boone, S. R.; Purser, G. H.; Chang, H.-R.; Lowery, M. D.; Hendrickson, D. N.; Pierpont, C. G. *J. Am. Chem. Soc.* **1989**, *111*, 2292. (j) Lah, M. S.; Kirk, M. L.; Hatfield, W.; Pecoraro, V. L. *J. Chem. Soc., Chem. Commun.* **1989**, 1606. (k) Drücke, S.; Wieghardt, K.; Nuber, B.; Weiss, J.; Bominaar, E. L.; Sawaryn, A.; Winkler, H.; Trautwein, A. X. *Inorg. Chem.* **1989**, *28*, 4477. (l) Sessler, J. L.; Silbert, J. W.; Lynch, V. *Inorg. Chem.* **1990**, *29*, 4143. (m) Sessler, J. L.; Hugdahl, J. D.; Lynch, V.; Davis, B. *Inorg. Chem.* **1991**, *30*, 334. (n) McCusker, J. K.; Vincent, J. B.; Schmitt, E. A.; Mino, M. L.; Shin, K.; Coggin, D. K.; Hagen, P. M.; Huffman, J. C.; Christou, G.; Hendrickson, D. N. *J. Am. Chem. Soc.* **1991**, *113*, 3012.

(10) Abbreviations include: Hacac, acetylacetone; HOBz, benzoic acid; HL-Bzim, 2,6-bis[bis((2-benzimidazolylmethyl)amino)methyl]-4-methylphenol; Hbimp, 2,6-bis[(bis((1-methylimidazol-2-yl)methyl)amino)methyl]-4-methylphenol; HBPMP, 2,6-bis[[bis(2-pyridylmethyl)amino]methyl]-4-methylphenol; H_3salmp, bis(salicylideneamino)-2-methylphenol; HDBM, dibenzoylmethane; HDPM, dipivaloylmethane; H_2acacen, *N,N'*-ethylenebis(acetylacetone imine); DBCatH_2, 3,5-di-*tert*-butylcatechol; H_5(HXTA), *N,N'*-(2-hydroxy-5-methyl-1,3-xylylene)bis(*N*-(carboxymethyl)glycine).

(11) Carnahan, E. M.; Rardin, R. L.; Bott, S. G.; Lippard, S. J. *Inorg. Chem.* **1992**, *31*, 5193.

(12) Lawton, S. L. *TRACER II, A FORTRAN Lattice Transformation-Cell Reduction Program*; Mobil Oil Corp.: Paulsboro, NJ, 1967.

(13) Sheldrick, G. M. In *Crystallographic Computing*; Sheldrick, G. M., C. Krüger, C., Goddard, R., Eds.; Oxford University Press: Oxford, 1985; p 175.

(14) Pathasarathi, V.; Beurskens, P. T.; Slot, H. J. B. *Acta Crystallogr.* **1983**, *A39*, 860.

(15) *TEXSAN: Single Crystal Structure Analysis Software, Version 5.0*; Molecular Structure Corp.: The Woodlands, TX, 1989.

(16) North, A. C. T.; Phillips, D. C.; Mathews, F. S. *Acta Crystallogr.* **1968**, *A24*, 351.

Table I. Crystallographic Information for $[Fe(OMe)(MeOH)(DPM)]_4$ (**1**), $[Fe(OMe)(MeOH)(DBM)]_4$·toluene, (**2**)·toluene, $[Fe_4(OMe)_5(MeOH)_3(OBz)_4]$·2MeOH, (**3**)·2MeOH, and $[Mn_4(OEt)_4(EtOH)_2(DPM)_4]$ (**4**)[a]

	1	**2**·toluene	**3**·2MeOH	**4**
formula	$Fe_4C_{52}H_{104}O_{16}$	$Fe_4C_{75}H_{80}O_{16}$	$Fe_4C_{38}H_{55}O_{18}$	$Mn_4C_{56}H_{108}O_{14}$
fw	1208.78	1460.84	1023.23	1225.24
cryst syst	monoclinic	triclinic	triclinic	triclinic
space group[b]	$P2_1/n$ (No. 14)	$P\bar{1}$ (No. 2)	$P\bar{1}$ (No. 2)	$P\bar{1}$ (No. 2)
a, Å	13.266(2)	14.912(3)	18.287(2)	13.902(2)
b, Å	31.243(2)	21.167(2)	21.747(2)	20.686(2)
c, Å	15.943 (2)	13.314 (2)	12.919 (1)	13.445 (1)
α, deg		93.81 (1)	105.14 (1)	108.496 (8)
β, deg	93.50 (1)	114.07 (1)	107.88 (1)	113.355 (8)
γ, deg		106.76 (1)	76.31 (1)	80.474 (9)
V, Å^3	6596 (1)	3592 (1)	4651 (1)	3362.6 (7)
Z	4	2	4	2
d_{calcd}, g cm^{-3}	1.217	1.351	1.461	1.211
T, K	195	195	188	188
data collctn range, deg	$3 \le 2\theta \le 46$	$3 \le 2\theta \le 50$	$4 \le 2\theta \le 50$	$3 \le 2\theta \le 46$
data limits	$+h, +k, \pm l$	$+h, \pm k, \pm l$	$\pm h, +k, \pm l$	$+h, \pm k, \pm l$
no. of data collected	10 238	14 067	17 703	10 425
R_{av}	0.023	0.024	0.052	0.028
no. of unique data	9339	12 555	16 322	9331
no. of obs unique data[c]	5829	7729	10 804	6117
no. of params	649	892	1081	663
data/param ratio	9.0	8.7	10.0	9.2
abs coeff, cm^{-1}	9.16	8.54	12.89	7.56
trans coeff, min/max	0.90/1.00	0.80/1.00	0.94/1.00	0.92/1.00
R[d]	0.043	0.045	0.053	0.042
R_w[d]	0.051	0.056	0.058	0.051
largest shift/esd, final	0.0003	0.002	0.002	0.04
largest peak, e/Å^3	0.46	0.57	0.71	0.50

[a] All measurements were made by using an Enraf Nonius CAD-4F κ-geometry diffractometer and Mo Kα (0.710 69 Å) radiation. [b] Hahn, T., Ed. *International Tables for X-ray Crystallography*; D. Reidel: Dordrecht, The Netherlands, 1983. [c] Observation criterion: $I > 3\sigma(I)$. [d] $R = \sum||F_o| - |F_c||/\sum|F_o|$ and $R_w = [\sum w(|F_o| - |F_c|)^2/\sum w|F_o|^2]^{1/2}$, where $w = 1/\sigma^2(F)$ and $\sigma^2(F)$ is defined in ref 11.

Examination of the crystal by ω-scans, $\Delta\bar{\omega}_{1/2} = 0.28°$, and axial photographs revealed the sample to be satisfactory for data collection. Study on the diffractometer revealed only $\bar{1}$ Laue symmetry, and the structure was refined in $P\bar{1}$. In the final stages of the structure solution, two toluene molecules were found in the crystal lattice; one, labeled C(100)–C(106), was located near an inversion center while the other, C(200)–C(203), was disordered about a center of symmetry. Since atoms in toluene C(100)′–C(106)′, generated by the inversion center, were within 1 Å of C(100) and C(101), this molecule was refined with half-occupancy. The final thermal parameters for these atoms were reasonable, supporting the model. For the second toluene molecule, three carbon atoms in the asymmetric unit, C(200), C(201), and C(202), were refined with full occupancy, and the site occupancy factor of the methyl substituent, C(203), was set equal to 0.5. Thus there are two complete toluene molecules in the unit cell. The largest peak in the final difference Fourier map was located near C(100), and had 0.57 e/Å^3.

$[Fe_4(OMe)_5(MeOH)_3(OBz)_4]$·2MeOH, (3)·2MeOH. X-ray quality, rectangular green crystals of **3**·2MeOH were obtained directly by the procedure described above. A crystal of dimensions 0.28 × 0.28 × 0.40 mm was mounted on a quartz fiber with a viscous hydrocarbon. Although the ω-scans for the sample were a little broad, $\Delta\bar{\omega}_{1/2} = 0.33°$, the peak profiles showed no fine structure. The Laue symmetry was $\bar{1}$, and space group $P\bar{1}$ was chosen. Two crystallographically independent molecules of **3** in the asymmetric unit were given the same labels with an asterisk used to distinguish them. The final shift/esd was 0.002, and the largest peak remaining in the final difference Fourier map was 0.71 e/Å^3, located near C(40) of a lattice solvent MeOH.

$[Mn_4(OEt)_4(EtOH)_2(DPM)_4]$ (4). A yellow block of approximate dimensions 0.41 × 0.32 × 0.30 mm was mounted on a glass fiber with Paratone N oil. An initial rotational photograph and mean peak widths, $\Delta\bar{\omega}_{1/2} = 0.26°$, indicated that the crystal diffracted well. Again space group $P\bar{1}$ was chosen. The structure was solved and refined in a straightforward manner, except for the two coordinated ethanol molecules. Close examination of difference Fourier maps in this region of the structure revealed two disordered ethyl groups. One was refined with two orientations, each at 50% occupancy, and the other with 75% and 25% site occupancy factors. Hydrogen atoms on all carbon atoms except for the disordered ethyl groups were included in calculated positions; the hydrogen atoms on the ethanol hydroxyl groups were located from a difference Fourier map. The largest remaining peak in the final difference Fourier map was 0.50 e/Å^3 and was located near one of the disordered ethanol ligands.

Physical Measurements. Electronic spectra were obtained on Perkin Elmer Lambda 7 and Cary 17D instruments. Deuterated solvents were used to examine the near-IR region for **3** to avoid the water vibrational overtones. The two low-energy bands in the spectrum of **3** were fit to Gaussian curves in order to determine their half-widths. An exponential function was included in the analysis to simulate the contribution to the absorbance from the more intense transitions below 350 nm. Fourier transform infrared spectra of KBr pellets were recorded on a Bio-Rad SPC3200 instrument.

Mössbauer spectra of polycrystalline samples of **1–3** dispersed in BN powder were obtained at various temperatures by using a conventional constant-acceleration spectrometer located at the Francis Bitter National Magnet Laboratory. The gamma ray source was ^{57}Co in Rh maintained at room temperature. Isomer shifts were referenced to iron metal at 300 K. Spectral parameters were determined by least-squares fitting of the experimental data to theoretically calculated spectra assuming Lorentzian line shapes.

Solid-state magnetic measurements of **1** (0.0339 g) and **3** (0.0627 g) were made using a Quantum Design SQUID susceptometer located in the Department of Materials Science and Engineering at M.I.T. The sample of **1** was compressed in a Teflon bucket with a plunger rod assembly to prevent potential rotation and orientation of the microcrystallites in the magnetic field during the measurement. More than 50 data points between 2.5 and 300 K for **3** and 20 and 300 K for **1** were collected at 3 kG. Below 20 K for **1**, a magnetic field of 0.5 kG was applied. The magnetism of the sample holders was measured at the same fields and temperatures and subtracted from the experimental values. Diamagnetic corrections of -7.2×10^{-4} and -4.6×10^{-4} emu mol^{-1} for **1** and **3**, respectively, were calculated from Pascal's constants and applied.[17]

DC magnetization studies of **1** at 1.2 K and **3** at 0.6 K from 0 to 20 T were performed at the Francis Bitter National Magnet Laboratory High-Field facility. A Bitter electromagnet and vibrating sample magnetometer were used.[18] As in the temperature-dependent susceptibility experiments, samples of **1** and **3**, weighing 0.0167 and 0.0177 g, respectively, were restrained in a Teflon bucket with a plunger rod. No

(17) (a) Carlin, R. L. *Magnetochemistry*; Springer-Verlag: New York, 1986. (b) O'Connor, C. J. *Prog. Inorg. Chem.* **1982**, *29*, 203.
(18) Foner, S. *Rev. Sci. Instrum.* **1959**, *30*, 548.

corrections for the negligible magnetic contributions of the sample holder nor for the inherent diamagnetism of the atoms were made to the magnetization values.

^{1}H NMR spectra of **1** and **2** were recorded on a Varian VXR-500 instrument in 90% C_6D_6/10% CD_3OD solutions. Chemical shifts were referenced to C_6D_6. The T_1 values were determined with an inversion-recovery pulse relaxation sequence followed by exponential fitting of the data.

Results and Discussion

Synthesis. A variety of synthetic routes are available for the preparation of metal alkoxide complexes, including reduction, substitution, and metathesis reactions.[19] For the synthesis of **1–4**, we used the metathesis procedure in which ferrous or manganous chloride was allowed to react with lithium alkoxide in the presence of the appropriate β-diketone or benzoic acid in an alcohol solvent. Addition of a second equivalent of lithium methoxide or ethoxide assured deprotonation of the chelating ligand. The overall stoichiometry of the reactions is summarized in eq 1.

$$MCl_2 + HL + 2LiOMe \xrightarrow{ROH} [M(OR)(L)]_n + 2LiCl \quad (1)$$

Complex	M	HL	ROH
1	Fe	HDPM	MeOH
2	Fe	HDBM	MeOH
3	Fe	HOBz	MeOH
4	Mn	HDPM	EtOH

During the synthesis of the iron β-diketonate complexes, a deep red (DPM) or blue (DBM) precipitate formed immediately upon addition of 2 equiv of lithium methoxide, and the solutions retained very little color. The yields were nearly quantitative prior to recrystallization. The two compounds could be readily recrystallized by layering methanol onto a saturated toluene solution, but solvents that did not include methanol failed to afford crystals of either complex. Both complexes are extremely air-sensitive, reacting instantaneously with dioxygen.

The synthetic procedure used to produce **1** and **2** follows closely that previously employed to obtain $[M(OMe)(MeOH)(acac)]_4$ complexes, where M = Co or Ni.[20] In these preparations, potassium hydroxide was used to deprotonate the alkoxide and β-diketonate ligands. Divalent metal–oxygen cubane complexes for the metals Mn, Co, Ni, and Cu have also been reported with a variety of other bridging and terminal ligands.[5,21] In order to evaluate the general utility of this synthetic route, we examined the corresponding reaction of $MnCl_2$ with HDPM in the presence of 2 equiv of LiOEt in ethanol. A light yellow solid precipitated immediately from the reaction mixture, leaving a colorless filtrate; the crude product was isolated in quantitative yield by filtration. Pure compound was obtained by layering EtOH on a solution of the compound in toluene, THF, or CH_2Cl_2. The product reacts instantaneously with dioxygen in solution, and within a few minutes in the solid state. Although more extensive physical and chemical characterizations of this and other manganese analogs are currently in progress,[22] we include the synthetic and structural results here to illustrate the ease and applicability of the synthetic procedure.

Use of benzoic acid in place of a β-diketone in the reaction with ferrous chloride produced a light orange solution and only a small amount of orange powder, which was removed by filtration. Following a procedure first used to prepare the mixed-valence polyiron oxo complex $[Fe_4^{III}Fe_8^{II}(O)_2(OMe)_{18}(OAc)_6(MeOH)_{4.67}]$ (**5**), the reaction solution was exposed to dry air over several days.[23] Slow diffusion of air into the reaction flask produced a green solution as iron(II) was oxidized to iron(III), and deep green crystals of $[Fe_4(OMe)_5(MeOH)_3(OBz)_4]\cdot 2MeOH$, (**3**)·2MeOH, precipitated. The ferrous ions could be oxidized more rapidly by adding air directly to the methanol solution, but a yellow precipitate, most likely an iron(III) alkoxide carboxylate, formed in addition to the crystals of **3**·2MeOH. The yield of the reaction based on iron was a modest 21%, but dioxygen is the limiting reagent for the reason noted above. The synthesis was quite reproducible, and sizable quantities of **3**·2MeOH were obtained in this manner. The complex is slightly air-sensitive and was therefore isolated under an inert atmosphere. The compound loses its crystallinity once removed from methanol, and the analytical data of the resulting green-blue powder are consistent with loss of two methanol molecules per iron alkoxide cube.

Few tetranuclear or high-nuclearity iron(II) or mixed-valent iron(II)/iron(III) complexes are known. One tetrairon(II) example, $[Fe_4(DBcat)_4(py)_6]$ (**6**), was prepared by alcoholysis of $[Fe\{N(SiMe_3)_2\}_2]$ with 3,5-di-*tert*-butylcatechol in the presence of pyridine, a metathesis reaction related to that employed in the syntheses of **1–3**.[8a] Three polynuclear mixed-valent iron–oxygen complexes are now available, two of which, **5** and $[Fe^{III}_{16}Fe^{II}(O)_{10}(OH)_{10}(OBz)_{20}]$ (**7**), arise from iron(II) or mixed-valent iron reagents upon introduction of air.[23,24] The third, $[Na_2\{Fe^{III}_2Fe^{II}_2(O)_2(acacen)_4\}]$ (**8**), was isolated upon reduction of a (μ-oxo)diiron(III) complex with sodium metal.[8c] Air oxidation has been used extensively in the preparation of high-nuclearity manganese complexes. As indicated in the introduction, many tetranuclear manganese complexes in a variety of oxidation states have been prepared in a search for a model of the OEC.[3,4,25]

Structural Studies. Figures 1–4 display ORTEP views of the four molecules. Complexes **1**, **2**·toluene, and **4** have quite similar structures, whereas the use of benzoate ligands and the presence of a single ferric site renders **3**·2MeOH unique. In all four molecules, the metal ions and bridging alkoxide ligands are located at alternating vertices of a cube. All metal ions are exclusively coordinated by oxygen donors.

The Fe(II) centers in **1** and **2** have almost identical octahedral coordination geometries. One octahedral face is occupied by three bridging methoxide ligands, and the other contains one chelating β-diketonate ligand and a methanol molecule. The arrangement of the terminal ligands around the $\{Fe_4(OMe)_4\}^{4+}$ core in both complexes is such that the point group symmetry is S_4. The symmetry-related bond lengths in **1** and **2** were identified by the letters *a*–*e* as indicated schematically in Figure 5. Selected average metrical parameters are compared for **1** and **2** in Table II. The related metal methoxide cubes, [M(OMe)(MeOH)-

(19) (a) Bradley, D. C.; Mehrotra, R. C.; Gaur, D. P. *Metal Alkoxides*; Academic Press: New York, 1978. (b) Mehrotra, R. C. *Adv. Inorg. Chem. Radiochem.* **1983**, *26*, 269. (c) Hubert-Pfalzgraf, L. G. *New J. Chem.* **1987**, *11*, 663. (d) Bradley, D. C. *Chem. Rev.* **1989**, *89*, 1317. (e) Caulton, K. G.; Hubert-Pfalzgraf, L. G. *Chem. Rev.* **1990**, *90*, 969.

(20) (a) Andrew, J. E.; Blake, A. B. *J. Chem. Soc. A* **1969**, 1456. (b) Bertrand, J. A.; Ginsberg, A. P.; Kaplan, R. I.; Kirkwood, C. E.; Martin, R. L.; Sherwood, R. C. *Inorg. Chem.* **1971**, *10*, 240.

(21) For examples, see (a) Co: Olmstead, M. M.; Power, P. P.; Siegel, G. A. *Inorg. Chem.* **1988**, *27*, 580. (b) Co, Ni: Paap, F.; Bouwman, E.; Driessen, W. L.; de Graaff, R. A. G.; Reedijk, J. *J. Chem. Soc. Dalton Trans.* **1985**, 737. (c) Ni: Gladfelter, W. L.; Lynch, M. W.; Schaefer, W. P.; Hendrickson, D. N.; Gray, H. B. *Inorg. Chem.* **1981**, *20*, 2390. (d) Ni: Boyd, P. D. W.; Martin, R. L.; Schwarzenbach, G. *Aust. J. Chem.* **1988**, *41*, 1449. (e) Ni: Bertrand, J. A.; Marabella, C.; Vanderveer, D. G. *Inorg. Chim. Acta* **1978**, *26*, 113. (f) Ni: Ballester, L.; Coronado, E.; Gutiérrez, A.; Monge, A.; Perpiñán, M. F.; Pinilla, E.; Rico, T. *Inorg. Chem.* **1992**, *31*, 2053. (g) Cu: Mergehenn, R.; Merz, L.; Haase, W.; Allmann, R. *Acta Crystallogr.* **1976**, *B32*, 505. (h) Cu: Schwabe, L.; Haase, W. *J. Chem. Soc. Dalton Trans.* **1985**, 1909. (i) Cu: Sletten, J.; Sørensen, A.; Julve, M.; Journaux, Y. *Inorg. Chem.* **1990**, *29*, 5054.

(22) Pence, L. E.; Lippard, S. J. Unpublished results.

(23) Taft, K. L.; Papaefthymiou, G. C.; Lippard, S. J. *Science* **1993**, *259*, 1302.

(24) (a) Micklitz, W.; Lippard, S. J. *J. Am. Chem. Soc.* **1989**, *111*, 6856. (b) Micklitz, W.; McKee, V.; Rardin, R. L.; Pence, L. E.; Lippard, S. J. Submitted for publication.

(25) (a) Debus, R. J. *Biochim. Biophys. Acta* **1992**, *1102*, 269. (b) Yachandra, V. K.; DeRose, V. J.; Latimer, M. J.; Mukerji, I.; Sauer, K.; Klein, M. P. *Science* **1993**, *260*, 675.

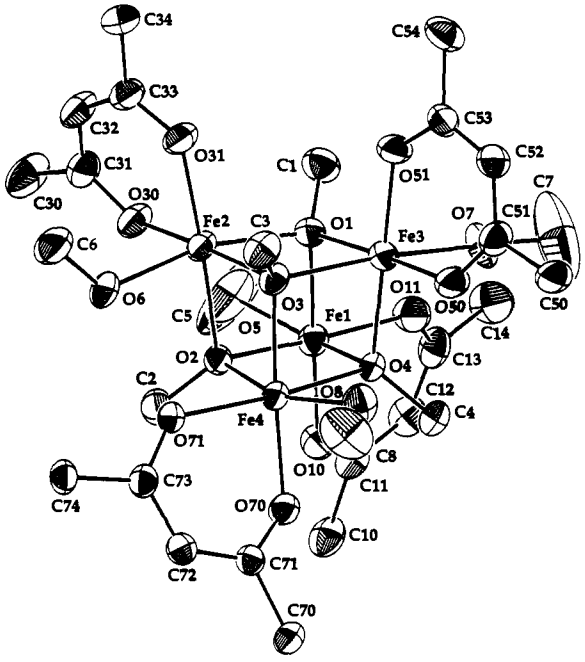

Figure 1. ORTEP view of $[Fe(OMe)(MeOH)(DPM)]_4$ (**1**) showing the 50% probability thermal ellipsoids. For clarity, the hydrogen atoms and methyl groups of the DPM ligands are omitted.

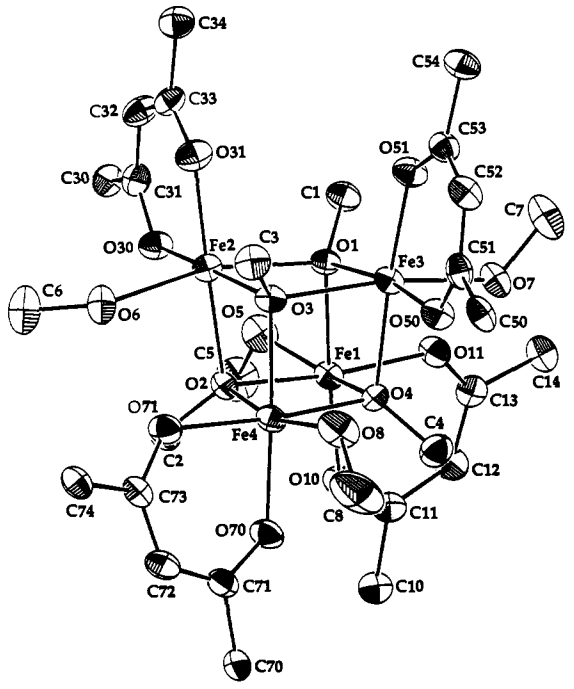

Figure 2. ORTEP view of $[Fe(OMe)(MeOH)(DBM)]_4$ (**2**) showing the 50% probability thermal ellipsoids. The hydrogens and phenyl carbon atoms, except for the first ring carbons, are omitted for clarity.

$(acac)]_4$ where M = Ni(II) or Co(II), have the same molecular symmetry.[20] The bond distances and angles around the ferrous ions in **1** and **2** are typical of those found in octahedrally coordinated high-spin iron(II) complexes with methoxide, β-diketonate, and methanol ligands.

There are subtle distortions in the iron coordination geometries for the different subsites of **1** and **2**, as can be judged by examining the average bond lengths in Table II. A significant tetragonal elongation occurs along the trans O–Fe–O bond vector involving the terminal methanol and bridging methoxide ligands, which produces distinct classes of Fe–O bond lengths. The four Fe–OMe bonds that lie perpendicular to the molecular S_4-axis and trans to the methanol ligands, designated *a* (Figure 5), are 0.05

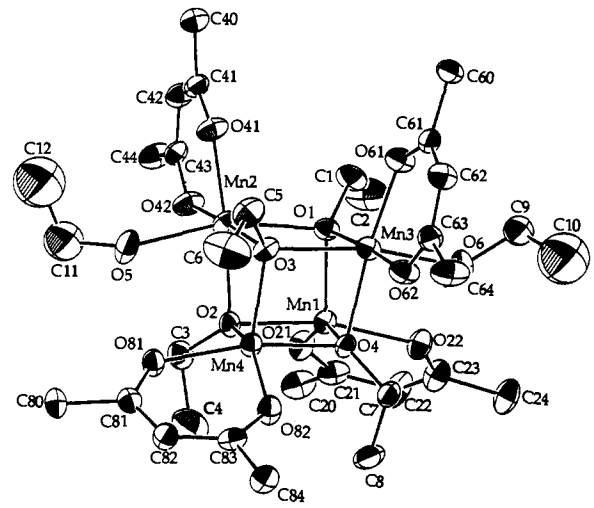

Figure 3. ORTEP view of $[Mn_4(OEt)_4(EtOH)_2(DPM)_4]$ (**4**) showing the 50% probability thermal ellipsoids. For clarity, the hydrogen atoms and methyl groups of the DPM ligands are omitted, and only one set of disordered ethanol molecules is depicted.

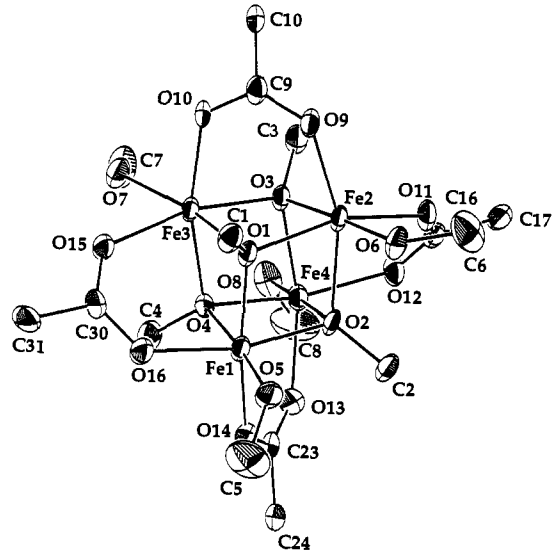

Figure 4. ORTEP view of one molecule of $[Fe_4(OMe)_5(MeOH)_3(OBz)_4]$ (**3**) in the asymmetric unit showing the 50% probability thermal ellipsoids. The hydrogen atoms and carbon atoms of the benzoate ligands, except for the carboxylate and first ring carbons, are omitted for clarity.

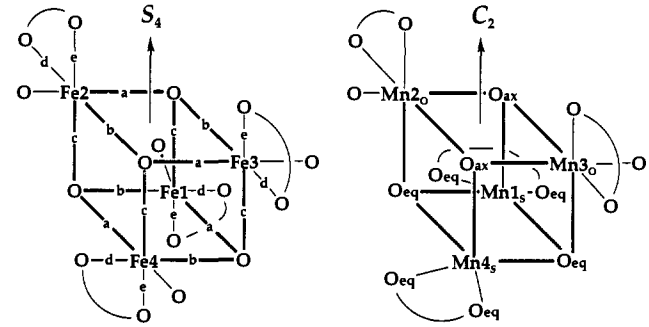

Figure 5. Idealized schematic of $\{M_4(OR)_4\}^{4+}$ cube structures for M = Fe, Mn. The unique distances are marked as described in the text, and the principal symmetry axis for each structure is noted.

and 0.097 Å longer in **1** and **2**, respectively, than the Fe–OMe distances *b*, which are perpendicular to the S_4-axis but trans to β-diketonate oxygen donors. The four Fe–OMe distances parallel to the S_4-axis, designated *c*, have similar bond lengths, slightly different from cube edges *a* and *b*. A distinction between the

Table II. Selected Average Bond Distances (Å) and Angles (deg) for $[Fe(OMe)(MeOH)(DPM)]_4$ (**1**) and $[Fe(OMe)(MeOH)(DBM)]_4$·toluene, (**2**)·toluene[a]

metrical parameter	1	2·toluene
Fe–OMe	2.13(3)	2.13(4)
a	2.16(1)	2.177(5)
b	2.11(1)	2.080(7)
c	2.11(2)	2.13(1)
Fe–O (β-diketonate)[b]	2.05(4)	2.04(2)
d	2.08(2)	2.06(1)
e	2.02(2)	2.028(6)
Fe–O(H)Me	2.24(2)	2.208(2)
MeO–Fe–OMe	82(1)	81(1)
Fe–OMe–Fe	98(2)	98(2)

[a] Values in parentheses are the standard deviations in the averaged metrical parameters. See Figure 5 for the labeling scheme employed. [b] The β-diketonate ligands are DPM for **1** and DBM for **2**.

Table III. Metal–Metal Distances (Å) in $[Fe(OMe)(MeOH)(DPM)]_4$ (**1**), $[Fe(OMe)(MeOH)(DBM)]_4$·toluene, (**2**)·toluene, $[Fe_4(OMe)_5(MeOH)_3(OBz)_4]$·2MeOH, (**3**)·2MeOH, and $[Mn_4(OEt)_4(EtOH)_2(DPM)_4]$ (**4**)[a]

		$[Fe(OMe)(MeOH)(DPM)]_4$ (**1**)			
Fe(1)	Fe(2)	3.166(1)	Fe(2)	Fe(3)	3.243(1)
Fe(1)	Fe(3)	3.152(1)	Fe(2)	Fe(4)	3.188(1)
Fe(1)	Fe(4)	3.259(1)	Fe(3)	Fe(4)	3.178(1)
		$[Fe(OMe)(MeOH)(DBM)]_4$·toluene, (**2**)·toluene			
Fe(1)	Fe(2)	3.208(1)	Fe(2)	Fe(3)	3.279(1)
Fe(1)	Fe(3)	3.201(1)	Fe(2)	Fe(4)	3.195(1)
Fe(1)	Fe(4)	3.229(1)	Fe(3)	Fe(4)	3.184(1)
		$[Fe_4(OMe)_5(MeOH)_3(OBz)_4]$·2MeOH, (**3**)·2MeOH			
Fe(1)	Fe(2)	3.298(1)	Fe(1)*	Fe(2)*	3.291(1)
Fe(1)	Fe(3)	3.073(1)	Fe(1)*	Fe(3)*	3.076(1)
Fe(1)	Fe(4)	3.103(1)	Fe(1)*	Fe(4)*	3.071(1)
Fe(2)	Fe(3)	3.055(1)	Fe(2)*	Fe(3)*	3.070(1)
Fe(2)	Fe(4)	3.089(1)	Fe(2)*	Fe(4)*	3.099(1)
Fe(3)	Fe(4)	3.292(1)	Fe(3)*	Fe(4)*	3.296(1)
		$[Mn_4(OEt)_4(EtOH)_2(DPM)_4]$ (**4**)			
Mn(1)	Mn(2)	3.225(1)	Mn(2)	Mn(3)	3.351(1)
Mn(1)	Mn(3)	3.147(1)	Mn(2)	Mn(4)	3.156(1)
Mn(1)	Mn(4)	3.277(1)	Mn(3)	Mn(4)	3.227(1)

[a] Numbers in parentheses are estimated standard deviations in the last significant digit.

Fe–O distances to the β-diketonate ligands is also evident, as revealed by comparing *d* and *e*. The oxygen atom of the β-diketonate ligand for distance *d* is intramolecularly hydrogen-bonded to the methanol ligand of an adjacent iron atom, one example being O(6)···O(71) (Figures 1 and 2). The average O···O distance for these interactions is 2.75(3) Å in both cubes, and the strong hydrogen-bond between these atoms lengthens *d* compared to *e*. As a result of these inequalities among the iron octahedra, the $\{Fe_4(OMe)_4\}^{4+}$ cores of **1** and **2** are expanded along the *a* edges of the cube.

The Fe···Fe vectors in the two complexes also reflect the alternating Fe–OMe bond lengths, as indicated in Table III. The two cube face diagonals perpendicular to the S_4-axis, Fe(1)···Fe(4) and Fe(2)···Fe(3), are an average of 0.08 and 0.05 Å longer in **1** and **2** than the four other face diagonal vectors. The four metal ions in the two cubes are thus compressed along the C_2-axis, lowering the Fe_4 symmetry from T_d to D_{2d}. Considering the entire $\{Fe_4(OMe)_4\}^{4+}$ core, the symmetry is further reduced to S_4 as a result of the inequivalent Fe–OMe bond distances. Almost all other structurally characterized $\{M_4(OR)_4\}^{4+}$ cubane complexes have similarly distorted metal ligand cores, although the specific geometric features for each complex vary. For example, the iron catecholate complex **6** has a more irregular structure, with two five- and two six-coordinate metal sites.[8a] The highest symmetry element in its $\{Fe_4(OR)_4\}^{4+}$ core is a C_2-axis. Moreover, the well-known $\{Fe_4S_4\}^{n+}$ class of compounds generally do not have T_d symmetry but belong to point group D_{2d} because of a compression along a C_2-axis similar to that occurring in **1** and **2**.[2] For these clusters, however, the iron atoms are four-coordinate; the tetrairon(II) analog of **1** or **2** is not yet known for iron complexes of the heavier chalcogenides.

Table IV. Selected Average Bond Distances (Å) and Angles (deg) for $[Mn_4(OEt)_4(EtOH)_2(DPM)_4]$ (**4**)[a]

metrical parameter	4	metrical parameter	4
Mn_O–OEt	2.21(2)	Mn_O–O(H)Et	2.296(2)
Mn_S–OEt_{ax}	2.089(6)	OEt–Mn_O–OEt	82(1)
Mn_S–OEt_{eq}	2.142(5)	OEt_{eq}–Mn_S–OEt_{ax}	86.6(9)
Mn_O–L	2.090(9)	OEt_{eq}–Mn_S–OEt_{eq}	80.2(1)
Mn_S–L_{long}	2.13(1)	Mn–OEt–Mn	83(3)
Mn_S–L_{short}	2.061(4)		

[a] Values in parentheses are the standard deviations in the averaged metrical parameters. See Figure 5 for the labeling scheme.

The $\{Mn_4(OEt)_4\}^{4+}$ core in **4** has many of the same geometric features found in **1** and **2**, except that two different types of manganese coordination environments are realized. For Mn(2) and Mn(3), octahedral coordination is preserved with an EtOH ligand occupying the sixth site. The Mn(1) and Mn(4) atoms lack the sixth ligand, however, displaying distorted square pyramidal geometry in which two oxygen atoms of the β-diketonate ligand and two oxygen atoms of the bridging ethoxides form the basal plane (Figures 3 and 5). The Mn atoms are displaced by 0.395(2) Å out of this plane. This second type of metal site lowers the symmetry from S_4 to C_2. Averaged values of related metrical parameters are listed in Table IV. The diagram in Figure 5 designates the local symmetry of the two types of metal sites, Mn_O and Mn_S for octahedral and square pyramidal atoms, respectively, as well as the axial (ax) and equatorial (eq) ligands in the square pyramids.

As a result of the different coordination numbers, the metal ligand distances at the cube subsites differ. For the octahedral Mn(2) and Mn(3) atoms, the distances to the bridging ethoxides are approximately equal, 2.21(2) Å, the DPM ligand forms a symmetrical chelate with Mn–O bonds averaging 2.090(9) Å, and the terminal ethanol ligand is at a relatively long distance of 2.296(2) Å. These values are similar to those in the Fe analogs, but without the tetragonal elongation. The coordination geometry about the distorted square pyramidal metals, Mn(1) and Mn(4), is substantially more irregular. The Mn–OEt distances are of two types; the axial bond is compressed to 2.089(6) Å compared to the average equatorial distances of 2.142(5) Å. The chelating DPM ligand is asymmetrically bound, with one Mn–O bond an average of 0.07 Å longer than the other. The coordinated ethanol ligands are hydrogen bonded to the DPM ligands of the distorted square pyramidal Mn atoms, O···O being 2.81(4) Å. As in the Fe cubes **1** and **2**, this interaction is responsible for the asymmetry of the chelate ring, the hydrogen-bonded Mn–O distances being longer.

The symmetry of the Mn_4 core in **4** is reduced from the idealized T_d to C_{2v} (Table III). The two M···M vectors perpendicular to the C_2 axis are significantly elongated, the distance between the octahedral Mn atoms being 3.351(1) Å and that between the square pyramidal Mn atoms being 3.277(1) Å. The other distances are significantly shorter, averaging 3.152(6) and 3.226(2) Å.

Other known Mn_4^{II} cubes display metal–metal distances in the range of 3.28 to 3.45 Å,[5,26] so **4** has shorter distances than observed previously for Mn_4 cubes of this oxidation state. Manganese displays a considerable flexibility in the cubic framework. In the (4+4) Schiff base macrocycle cubes,[5] the metals are seven-coordinate. Octahedral coordination is the most common both in discrete cubes and in cuboidal fragments within larger polymanganese clusters.[6,27] Tetrahedral subsite coordination

(26) Stephan, H.-O.; Chen, C.; Henkel, G.; Griesar, K.; Haase, W. *J. Chem. Soc., Chem. Commun.* **1993**, 886.

Table V. Average Bond Distances (Å) and Angles (deg) for $[Fe_4(OMe)_5(MeOH)_3(OBz)_4]\cdot 2MeOH$, (3)·2MeOH[a]

Fe(1)	O(1)	2.05(2)	Fe(3)	O(1)	2.15(1)
Fe(1)	O(2)	2.04(2)	Fe(3)	O(3)	2.099(9)
Fe(1)	O(4)	2.09(3)	Fe(3)	O(4)	2.128(8)
Fe(1)	O(5)	1.94(5)	Fe(3)	O(7)	2.149(8)
Fe(1)	O(14)	2.049(8)	Fe(3)	O(10)	2.09(1)
Fe(1)	O(16)	2.040(8)	Fe(3)	O(15)	2.11(3)
Fe(2)	O(1)	2.14(2)	Fe(4)	O(2)	2.15(2)
Fe(2)	O(2)	2.14(2)	Fe(4)	O(3)	2.16(1)
Fe(2)	O(3)	2.10(1)	Fe(4)	O(4)	2.107(8)
Fe(2)	O(6)	2.09(5)	Fe(4)	O(8)	2.15(1)
Fe(2)	O(9)	2.10(3)	Fe(4)	O(12)	2.06(2)
Fe(2)	O(11)	2.08(4)	Fe(4)	O(13)	2.12(1)
O(1)	Fe(1) O(2)	77.8(6)	O(1)	Fe(2) O(2)	74(1)
O(1)	Fe(1) O(4)	86.5(3)	O(1)	Fe(2) O(3)	86.1(6)
O(1)	Fe(1) O(5)	97(1)	O(1)	Fe(2) O(6)	94(2)
O(1)	Fe(1) O(14)	165.9(8)	O(1)	Fe(2) O(9)	88(1)
O(1)	Fe(1) O(16)	89.3(4)	O(1)	Fe(2) O(11)	161(1)
O(2)	Fe(1) O(4)	85.6(4)	O(2)	Fe(2) O(3)	86(1)
O(2)	Fe(1) O(5)	97.3(4)	O(2)	Fe(2) O(6)	92(1)
O(2)	Fe(1) O(14)	89.7(6)	O(2)	Fe(2) O(9)	161(3)
O(2)	Fe(1) O(16)	165.1(7)	O(2)	Fe(2) O(11)	88.3(5)
O(4)	Fe(1) O(5)	176(1)	O(3)	Fe(2) O(6)	178.1(4)
O(4)	Fe(1) O(14)	86(1)	O(3)	Fe(2) O(9)	88.5(2)
O(4)	Fe(1) O(16)	86.3(4)	O(3)	Fe(2) O(11)	88(2)
O(5)	Fe(1) O(14)	90.9(5)	O(6)	Fe(2) O(9)	93.3(4)
O(5)	Fe(1) O(16)	91.6(4)	O(6)	Fe(2) O(11)	91.1(4)
O(14)	Fe(1) O(16)	102(2)	O(9)	Fe(2) O(11)	110(4)
O(1)	Fe(3) O(3)	86(1)	O(2)	Fe(4) O(3)	85(1)
O(1)	Fe(3) O(4)	83(1)	O(2)	Fe(4) O(4)	82(2)
O(1)	Fe(3) O(7)	172(1)	O(2)	Fe(4) O(8)	176(1)
O(1)	Fe(3) O(10)	89(3)	O(2)	Fe(4) O(12)	89(1)
O(1)	Fe(3) O(15)	88(2)	O(2)	Fe(4) O(13)	88(1)
O(3)	Fe(3) O(4)	78.6(4)	O(3)	Fe(4) O(4)	77.8(2)
O(3)	Fe(3) O(7)	100(2)	O(3)	Fe(4) O(8)	97(3)
O(3)	Fe(3) O(10)	88.7(6)	O(3)	Fe(4) O(12)	88.6(6)
O(3)	Fe(3) O(15)	165(1)	O(3)	Fe(4) O(13)	163.1(7)
O(4)	Fe(3) O(7)	100(5)	O(4)	Fe(4) O(8)	100(2)
O(4)	Fe(3) O(10)	165.5(3)	O(4)	Fe(4) O(12)	164.4(4)
O(4)	Fe(3) O(15)	87(1)	O(4)	Fe(4) O(13)	87(1)
O(7)	Fe(3) O(10)	89(4)	O(8)	Fe(4) O(12)	89.2(4)
O(7)	Fe(3) O(15)	88(3)	O(8)	Fe(4) O(13)	91(3)
O(10)	Fe(3) O(15)	105(1)	O(12)	Fe(4) O(13)	106.2(4)
Fe(1)	O(1) Fe(2)	103.7(4)	Fe(2)	O(3) Fe(3)	93.7(6)
Fe(1)	O(1) Fe(3)	94.3(4)	Fe(2)	O(3) Fe(4)	93(1)
Fe(1)	O(1) C(1)	120.9(7)	Fe(2)	O(3) C(3)	117.9(6)
Fe(2)	O(1) Fe(3)	91(1)	Fe(3)	O(3) Fe(4)	101.4(2)
Fe(2)	O(1) C(1)	121.5(6)	Fe(3)	O(3) C(3)	122(2)
Fe(3)	O(1) C(1)	118.7(6)	Fe(4)	O(3) C(3)	122.0(6)
Fe(1)	O(2) Fe(2)	104.2(4)	Fe(1)	O(4) Fe(3)	93.7(9)
Fe(1)	O(2) Fe(4)	95(1)	Fe(1)	O(4) Fe(4)	95(2)
Fe(1)	O(2) C(2)	120.2(6)	Fe(1)	O(4) C(4)	120.9(8)
Fe(2)	O(2) Fe(4)	92(1)	Fe(3)	O(4) Fe(4)	102.2(2)
Fe(2)	O(2) C(2)	121.4(9)	Fe(3)	O(4) C(4)	121(2)
Fe(4)	O(2) C(2)	117.9(6)	Fe(4)	O(4) C(4)	119.0(7)
Fe(1)	O(5) C(5)	124.7(8)	Fe(3)	O(7) C(7)	131.7(8)
Fe(2)	O(6) C(6)	124.2(8)	Fe(4)	O(8) C(8)	118.0(8)

[a] Numbers in parentheses are estimated standard deviations in the averaged values.

occurs in $[Mn_4Te_4(TePr^i)_4]^{4-}$.[26] Compound **4** is an unusual example in that it has distorted square pyramidal Mn coordination in a cube as well as metals possessing two different coordination numbers.

The mixed-valent iron methoxide cube **3** is less symmetric than complex **1**, **2**, or **4**. Two discrete molecules of **3** are present in the asymmetric unit with essentially identical structures. We therefore discuss their metrical parameters together and have labeled them identically, distinguishing different molecules where required with an asterisk. Average bond distances and angles are compiled in Table V. The core of **3** contains four iron atoms and four methoxide bridges, as in **1** and **2**. Four benzoate bridges, which span cube diagonals, replace the β-diketonate chelate ligands of the tetrairon(II) cubes, and a single iron site, Fe(1), is oxidized by one electron. The unique ferric center was identified by comparing the average Fe–O bond lengths, which for Fe(1) are 2.03(5) Å and for Fe(2), Fe(3), and Fe(4) are 2.12(4) Å. The compound is therefore valence-localized. Moreover, the terminal alcohol ligand at the iron(III) site in **3** is deprotonated. The Fe(1)–O(5) distance of 1.94(4) Å may be compared to an average iron(II)–methanol bond distance of 2.13(4) Å. The length of an iron(III)–methanol bond is greater than 2.1 Å.[28] The orientation of the four carboxylate ligands and the presence of a ferric site reduce the symmetry of the molecule to C_1.

The benzoate bridges and ferric ion cause considerable distortion in the $\{Fe_4(OMe)_4\}^{5+}$ core. The average Fe–OMe distances for the iron(II) and iron(III) sites are 2.13(3) and 2.06(3) Å, respectively, distorting the cube inward toward Fe(1) at three of its corners. Moreover, the Fe···Fe distances across cube diagonals bridged by the benzoate ligands are shortened (Table III). Metal–metal vectors lying in cube faces having just two bridging methoxides, Fe(1)···Fe(2) and Fe(3)···Fe(4) (Figure 4), average 3.294(3) Å, whereas, for the bis(μ-methoxo)(μ-carboxylato)diiron pairs, the Fe···Fe distances average 3.08(2) Å. The interior angles, MeO–Fe–OMe and Fe–OMe–Fe, have values ranging from 72.9(1) to 97.9(2)° and 90.2(1) to 104.4(2)°, respectively. They can be classified into two groups, those lying in cube faces spanned by a benzoate bridge and those in cube faces having just two methoxide bridges. The OMe–Fe–OMe and Fe–OMe–Fe angles of the triply-bridged faces measure 85(2) and 94(2)°, whereas the same angles in the doubly-bridged cube faces average 77(2) and 103(1)°. The Fe–OMe–Fe–OMe parallelepipeds comprising each cube face are therefore geometrically closer to a square for those spanned by a benzoate bridge and better approximate a parallelogram when there is no such bridging ligand (Figure 4).

Of the three mixed-valent polyiron complexes having at least four iron atoms, complexes **5** and heptadecanuclear complex **7** contain cubane units. Two corner-sharing $\{\{Fe_3(O)_3(OH)\}_2M\}^{6+}$ cubes constitute the core of complex **7**,[24] and the iron oxo/alkoxide structure of **5** can be considered as the fusion of four $\{Fe(O)(OMe)_3\}^{n+}$ cubes.[23] In addition, a discrete mixed-valent cube has been isolated for cobalt, $[Co^{III}_2Co^{II}_2(OMe)_4(OAc)_2(acac)_4]$. Its structure, like that of **3**, is severely distorted owing to the presence of bridging acetate ligands.[29]

One additional feature of the structure of **3** deserves comment. Terminal methoxide ligands coordinated to iron are rare. To the best of our knowledge, there is only one previously reported example.[30] Terminal hydroxide ligands are unknown in iron chemistry, being unstable with respect to deprotonation and formation of multiply-bridging oxo groups. The alkyl substituent presumably allows the methoxide analog to be isolated. The average Fe(1)–O(5) distance in **3**, 1.94(4) Å, may be compared to an average Fe(III)–OMe distance of 1.87(2) Å in $[Fe_6O(OMe)_{18}]^{2+}$.[30] The slightly longer distance for **3** may be due to hydrogen-bonding between the methanol lattice molecules and the terminal methoxide ligands. The O···O distance for these interactions is quite short, averaging 2.52(3) Å. The short Fe–OMe distance generates a trans influence in **3**, the trans Fe(1)–OMe distance being 0.05 Å longer than Fe–(OMe) bond lengths trans to methanol or benzoate ligands.

Solution Stability and Electronic Spectral Properties. The cubane complexes have rich electronic spectra, displaying multiple absorptions giving rise to the intense red, blue, green, and yellow colors of **1**–**4**. The stability in solution of the tetrairon(II) cubes **1** and **2** and the tetramanganese(II) cube **4** is extremely dependent

(27) Sessoli, R.; Tsai, H.-L.; Schake, A. R.; Wang, S.; Vincent, J. B.; Folting, K.; Gatteschi, D.; Christou, G.; Hendrickson, D. N. *J. Am. Chem. Soc.* **1993**, *115*, 1804.

(28) Taft, K. L.; Garfinkel-Shweky, D.; Masschelein, A.; Liu, S.; Bino, A.; Lippard, S. J. *Inorg. Chim. Acta* **1992**, *198–200*, 627.

(29) Bertrand, J. A.; Hightower, T. C. *Inorg. Chem.* **1973**, *12*, 206.

(30) Hegetschweiler, K.; Schmalle, H. W.; Streit, H. M.; Gramlich, V.; Hund, H.-U.; Erni, I. *Inorg. Chem.* **1992**, *31*, 1299.

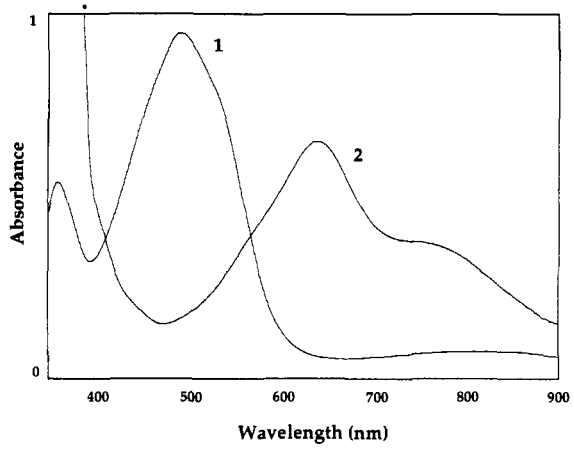

Figure 6. UV–visible electronic spectra of $[Fe(OMe)(MeOH)(DPM)]_4$ (**1**) and $[Fe(OMe)(MeOH)(DBM)]_4$ (**2**) in 90% toluene/10% MeOH. The concentrations were 0.376 and 0.116 mM, respectively.

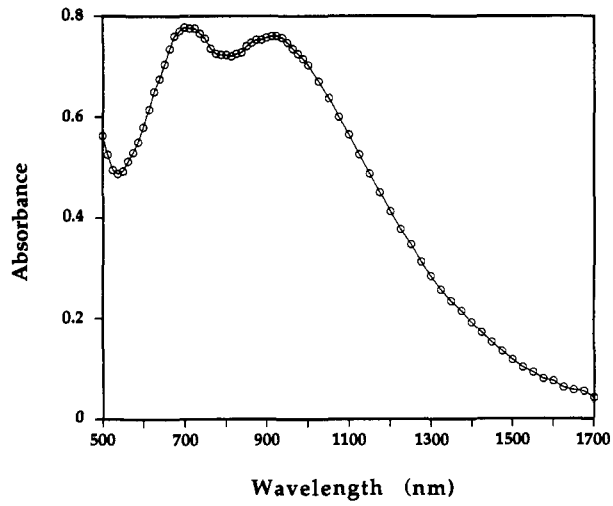

Figure 7. Near-IR–vis electronic spectrum of $[Fe_4(OMe)_5(MeOH)_3(OBz)_4]$ (**3**) in 50% CD_2Cl_2/50% CD_3OD at a concentration of 2.58 mM.

on solvent conditions; the compounds decompose or isomerize in all pure solvents in which they are soluble. For example, the most intense transition in the visible region for both complexes **1** and **2** shifted to lower wavelengths in either THF or toluene over a period of several hours. Several isosbestic points were observed during this transformation, but the reaction products have not yet been identified. Stable, reproducible spectra having absorbance features that obeyed Beer's Law were obtained for the two complexes in solutions of composition 90% toluene/10% MeOH. Representative spectra are given in Figure 6. Similar spectra were obtained at all ratios examined for these two solvents. Methanol stabilizes the iron methoxide cubes, and the failure to grow crystals of either complex in its absence reinforces this observation. Interestingly, the iron methoxide cube **1** is unstable in other solvent/MeOH mixtures. The initial spectrum of **1** in 50% CH_2Cl_2/50% MeOH was identical to that recorded in toluene/MeOH, but the absorbance features gradually changed, albeit more slowly, as was the case in pure CH_2Cl_2. In THF/MeOH solutions, the complex began to decompose immediately. The mixed-valent complex **3** tolerated a larger range of solvents. Its spectral features were measured in a CH_2Cl_2/MeOH mixture, and the complex appeared to survive pure DMF, CH_2Cl_2, or toluene.

Intense metal–ligand charge-transfer transitions are present in the UV region for all four complexes. These absorption bands occur below 350 nm and tail into the visible region. The transition at 301 nm for **4** is responsible for its bright yellow color, and there are no other features observed up to 900 nm, as expected for high-spin d^5 ions. Other iron and manganese alkoxide complexes have similar strong UV absorbances.[31-33]

All three iron complexes have a spectral feature between 700 and 850 nm, which we attribute to a spin-allowed d–d transition of the iron(II) ions. For a high-spin d^6 ion with O_h symmetry, this feature would correspond to the $^5T_{2g} \rightarrow {}^5E_g$ transition.[34] Tetragonal distortion (D_{4h}) of the ferrous subsites splits the excited ^5E_g state into $^5A_{1g}$ and $^5B_{1g}$ states. The degeneracy of the ground state is also partially removed by the distortion. This splitting is not often resolved by electronic spectroscopy, however. In the Mössbauer spectra of **1**, the temperature dependence of the quadrupolar splitting parameter indicates the presence of low-lying excited levels in the T_{2g} manifold, as discussed below. Bands arising from the two excited states are observed for **1**, the transition to $^5B_{1g}$ occurring at 810 nm (12 340 cm^{-1}) and to $^5A_{1g}$ at 1125 nm (8900 cm^{-1}). For **2** and **3**, the transition to $^5B_{1g}$ is observed at 780 (12 820 cm^{-1}) and 705 nm (14 180 cm^{-1}), respectively, whereas the $^5A_{1g}$ component is obscured by other absorption features. These energies are slightly higher than those found for a series of $[Fe(H_2O)_4X_2]$ complexes,[34b] because the negatively charged oxygen atom donor ligands in the iron methoxide cubes provide a larger crystal field splitting than water and halide ligands. Other octahedrally coordinated iron(II) complexes have similar absorption bands. In the bis(μ-aryloxo)diiron(II) complex $[Fe^{II}_2(salmp)_2]^{2-}$, for example, a feature occurring at 800 nm was assigned as a transition to the ^5E_g state.[31] The mineral vivianite, which contains $Fe^{II}O_6$ octahedra, has two bands at 1200 and 880 nm that have also been assigned to spin-allowed transitions.[35] Features at 820 and 1000 nm were assigned to the $^5T_{2g} \rightarrow {}^5E_g$ transition in the homoleptic complexes $[Fe(acac)_2]$ and $[Fe(OMe)_2]$, respectively.[36]

Intense absorption bands occur in the visible region of **1** and **2** which are absent in **3** and therefore attributable to transitions involving the β-diketonate ligands. From their intensity, these absorptions are tentatively assigned to metal $\rightarrow$ ligand charge-transfer transitions, from the partially filled d-orbitals of the ferrous ions to the π^* level orbitals of the ligands. Related transitions are known for high-spin Fe(II)–pyridine complexes.[37] The absorptions are shifted to longer wavelengths in the case of **2**. The phenyl ring is inductively electron-withdrawing compared to the *tert*-butyl substituent, and any potential conjugation of phenyl moieties with the β-diketonate π framework would also diminish the energy of the π^* levels. The availability of several π^* orbitals of the β-diketonate ligands may account for the presence of multiple visible bands.

As shown in Figure 7, the mixed-valent iron methoxide cube has an additional absorption at 925 nm in 50% CD_2Cl_2/50% CD_3OD solutions which shifts below 900 nm in 50% C_6D_6/50% CD_3OD. The breadth of this peak and its solvent dependence identifies it as an intervalence charge-transfer (IVCT) transition.[38] The extinction coefficient, $\epsilon = 295\ M^{-1}\ cm^{-1}$, is consistent with those reported for other IVCT transitions in dinuclear iron(II,-

(31) Snyder, B. S.; Patterson, G. S.; Abrahamson, A. J.; Holm, R. H. *J. Am. Chem. Soc.* **1989**, *111*, 5214.
(32) Dong, Y.; Ménage, S.; Brennan, B. A.; Elgren, T. E.; Jang, H. G.; Pearce, L. L.; Que, L., Jr. *J. Am. Chem. Soc.* **1993**, *115*, 1851.
(33) Bochman, M.; Wilkinson, G.; Young, G. B.; Hursthouse, M. B.; Malik, K. M. A. *J. Chem. Soc. Dalton Trans.* **1980**, 1863.
(34) (a) Figgis, B. N. *Introduction to Ligand Fields*; Interscience Publishers: New York, 1966. (b) Lever, A. B. P. *Inorganic Electronic Spectroscopy*, 2nd ed.; Elsevier: New York, 1984.
(35) (a) Burns, R. G. *Annu. Rev. Earth Planet. Sci.* **1981**, *9*, 345. (b) Amthauer, G.; Rossman, G. R. *Phys. Chem. Minerals* **1984**, *11*, 37.
(36) (a) Adams, R. W.; Bishop, E.; Martin, R. L.; Winter, G. *Aust. J. Chem.* **1966**, *19*, 207. (b) Buckingham, D. A.; Gorges, R. C.; Henry, J. T. *Aust. J. Chem.* **1967**, *20*, 281.
(37) Borovik, A. S.; Hendrich, M. P.; Holman, T. R.; Münck, E.; Papaefthymiou, V.; Que, L., Jr. *J. Am. Chem. Soc.* **1990**, *112*, 6031.
(38) (a) Allen, G. C.; Hush, N. S. *Prog. Inorg. Chem.* **1967**, *8*, 357. (b) Hush, N. S. *Prog. Inorg. Chem.* **1967**, *8*, 391.

III) systems.[39] The observed spin-allowed and IVCT spectral bands of **3** in the 500–1800 nm region were fit to two Gaussian band shapes in order to determine their bandwidths. An exponential tail at the high-energy end of the spectral range was included to simulate the contribution from intense bands below 500 nm. From this fit, a bandwidth at half-height, $\Delta\nu_{1/2}$, of 7 600 cm^{-1} was determined for the IVCT transition. The theoretical value of $\Delta\nu_{1/2}$ is related to the energy of the transition, E_{OP}, according to eq 2.[38] The theoretical value of $\Delta\nu_{1/2}$ for an

$$\Delta\nu_{1/2} = \sqrt{2.31 \times 10^3 E_{OP}} \qquad (2)$$

E_{OP} of 10 800 cm^{-1} (925 nm) is 5000 cm^{-1}, significantly less than that estimated for **3**. Although the ratio of observed to calculated $\Delta\nu_{1/2}$ values for weakly to moderately coupled dinuclear mixed-valent complexes is often greater than 1, a value of 1.3 having been found for other cases,[39c,40] the ratio for **3** is more than 1.5. The occurrence of two distinct Fe···Fe distances in the iron methoxide core may be the reason for the large $\Delta\nu_{1/2}$ value. At least two IVCT transitions probably contribute to the single absorbance feature in the near-IR region. In addition, other bands are most likely present in this absorption envelope which were not accounted for in the analysis, including the second component of the spin-allowed transition for the ferrous ions and spin-forbidden transitions for both iron(II) and iron(III). The IVCT transition may appear artificially broad owing to these other contributions.

The high energy of the IVCT band in **3** is unusual in complexes with Fe–O bonds. A large number of (μ-phenoxo)bis(μ-carboxylato)diiron(II,III) complexes have IVCT transitions with E_{OP} less than 8000 cm^{-1}.[39] One exception is $[Fe^{II}Fe^{III}(HXTA)(OAc)_2]^{2-}$, for which two features, with E_{OP} equal to 11 900 and 7 800 cm^{-1}, were assigned as IVCT transitions.[39a] The source of the high E_{OP} value in **3** is uncertain. The above examples all have a single monoatomic bridge, whereas two bridging methoxide ligands occur in **3**, resulting in correspondingly shorter Fe···Fe distances. The energy for the IVCT transition in the edge-shared iron dimer $[Fe^{III}Fe^{II}(salmp)_2]^-$, a bis($\mu$-aryloxo)diiron(II,III) complex with an Fe···Fe distance of 3.1 Å, however, is 7 700 cm^{-1}.[31] Edge-shared mixed-valent iron-containing minerals exhibit IVCT transitions with $E_{OP} > 13\,000$ cm^{-1}. For partially oxidized forms of vivianite, which has a bis(μ-hydroxo)diiron(III,II) core, an intense absorption at 15 870 cm^{-1} has been attributed to the interchange of electrons between the two iron sites.[35]

From the analysis of the X-ray structure and the IVCT transition, we assign complex **3** to Class II in the Robin and Day scheme for mixed-valent species.[41] This designation is corroborated by variable-temperature Mössbauer investigations discussed below.

^{1}H NMR Spectroscopy. The ^{1}H NMR spectra of **1** and **2** obtained in 90% C_6D_6/10% CD_3OD are consistent with the structures determined in the solid state by X-ray methods (Figure S1, supplementary material). Methanol was added to stabilize the iron alkoxide cubes, as discussed above. Exchange of the bridging methoxide and terminal methanol ligands with CD_3OD diminished the intensities of these resonances, and proton resonances from the liberated CH_3OH protons were observed in the spectra of the two compounds at approximately 3.4 and 4.5 ppm. The remaining resonances, located between 2 and 20 ppm, are attributed to the β-diketonate ligands of the two complexes. The signals are relatively sharp because high-spin iron(II) complexes typically display well-resolved spectra due to favorable relaxation times.[42]

The proton resonances for the DBM and DPM ligands in **1** and **2** were assigned by a comparison of their chemical shifts in the $\{Fe_4(OCD_3)_4\}^{4+}$ cubes with those of other ferrous complexes, by their T_1 values, and by their integrated intensities. The four β-diketonate ligands are related by a molecular S_4 symmetry axis. The single methine proton of both the DPM and DBM complexes occurs at 14 ppm in the spectra. The methyl substituents of the DPM ligand in **1** resonate at 3.31 ppm, overlapping with the methyl signal of free methanol. The two resonances were distinguished by the fact that their T_1 values differed by 2 orders of magnitude, the faster relaxing protons being assigned to the DPM ligand. The phenyl protons for DBM are grouped between 16 and 19 ppm. No other signals are observed in the ±100-ppm range for **2**, so two of the phenyl ring protons must have very similar chemical shifts. Assigning these features is difficult without deuterium substitution of the ligand.

The ^{1}H NMR and electronic spectral studies indicate that the iron methoxide cubes are stable in solvent mixtures that contain methanol. Proton NMR spectra of **1** in pure C_6D_6 displayed too many resonances for a cube structure, indicating that the $\{Fe_4(OMe)_4\}^{4+}$ core decomposes or isomerizes under these conditions. A more detailed assessment of the NMR spectra of these iron alkoxide cubes, including the dipolar and contact shift contributions to the isotropic shifts, the relaxation characteristics, and the rate of ligand exchange, requires additional study.[43]

Mössbauer Spectroscopy. Mössbauer spectra of polycrystalline and frozen solution samples of **1–3** are presented in Figures 8 and 9. Parameters used to fit the spectra are compiled in Table VI, along with those of other diiron(II) and mixed-valent iron complexes.[23,39,44,45] For the two iron(II) cubes, a single quadrupole doublet is observed in the solid-state spectra at 80 K (Figure 8). Although there are four crystallographically unique iron sites in these complexes, their nearly identical coordination environments produce unresolved Mössbauer spectra, resulting in a single, broad quadrupole doublet. The isomer shift, δ, and quadrupole splitting parameters, ΔE_Q, for **1** and **2** are consistent with those found for high-spin iron(II) complexes.

The mixed-valent iron methoxide cube **3** exhibits well-resolved iron(III) and iron(II) spectral subcomponents at 80 K in the solid state, as shown in Figure 9. As was the case for **1** and **2**, the unique iron(II) sites in the asymmetric unit of **3** fall under a single absorption envelope. A two-site fit of the spectra gave an absorption ratio of 1:3 for iron(III):iron(II), confirming the oxidation state assignments made in the structural study and the analysis of the electronic spectrum of the $\{Fe_4(OMe)_4\}^{5+}$ cube. The isomer shifts determined for the iron atoms in **3** are consistent with those measured for other mixed-valent iron compounds, the quadrupole splitting parameters for which have a large range. The polyiron oxo complex **5**, which contains cubane fragments like those in the discrete complex **3**, has similar Mössbauer spectral parameters (Table VI). The ΔE_Q value for the single iron(II) site in **3** falls between those of the two ferrous doublets observed in **5**.[23]

The frozen solution Mössbauer spectra of complexes **2** and **3** were also studied in solvent mixtures containing methanol and either toluene or CH_2Cl_2 (Figures 8 and 9). The isomer shifts and quadrupole splittings of the solid and solution spectra are identical for **2** and quite similar for **3**. The small feature in the spectrum of **2** at approximately 0.7 mm s^{-1} is due to an iron(III)

(39) (a) Borovik, A. S.; Murch, B. P.; Que, L., Jr.; Papaefthymiou, V.; Münck, E. *J. Am. Chem. Soc.* **1987**, *109*, 7190. (b) Suzuki, M.; Oshio, H.; Uehara, A.; Endo, K.; Yanaga, M.; Kida, S.; Saito, K. *Bull. Chem. Soc. Jpn.* **1988**, *61*, 3907. (c) Borovik, A. S.; Papaefthymiou, V.; Taylor, L. F.; Anderson, O. P.; Que, L., Jr. *J. Am. Chem. Soc.* **1989**, *111*, 6183. (d) Mashuta, M. S.; Webb, R. J.; McCusker, J. K.; Schmitt, E. A.; Oberhausen, K. J.; Richardson, J. F.; Buchanan, R. M.; Hendrickson, D. N. *J. Am. Chem. Soc.* **1992**, *114*, 3815.

(40) Curtis, J. C.; Meyer, T. J. *J. Am. Chem. Soc.* **1978**, *100*, 6284.

(41) Robin, M. B.; Day, P. *Adv. Inorg. Chem. Radiochem.* **1967**, *10*, 247.

(42) Wu, F. J.; Kurtz, D. M., Jr. *J. Am. Chem. Soc.* **1989**, *111*, 6563.

(43) Ming, L.-J.; Jang, H. G.; Que, L., Jr. *Inorg. Chem.* **1992**, *31*, 359.

(44) Surerus, K. K.; Münck, E.; Snyder, B. S.; Holm, R. H. *J. Am. Chem. Soc.* **1989**, *111*, 5501.

(45) Tolman, W. B.; Liu, S.; Bentsen, J. G.; Lippard, S. J. *J. Am. Chem. Soc.* **1991**, *113*, 152.

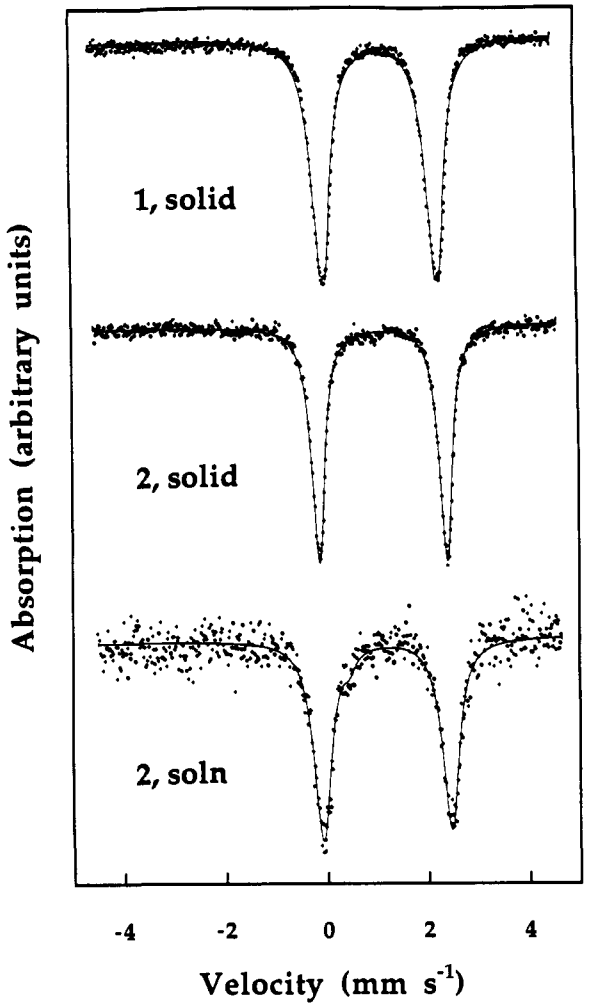

Figure 8. Mössbauer spectra at 80 K of polycrystalline [Fe(OMe)(MeOH)(DPM)]$_4$ (1) (top) and [Fe(OMe)(MeOH)(DBM)]$_4$ (2) (middle) and 2 in a 90% toluene/10% MeOH solution (bottom).

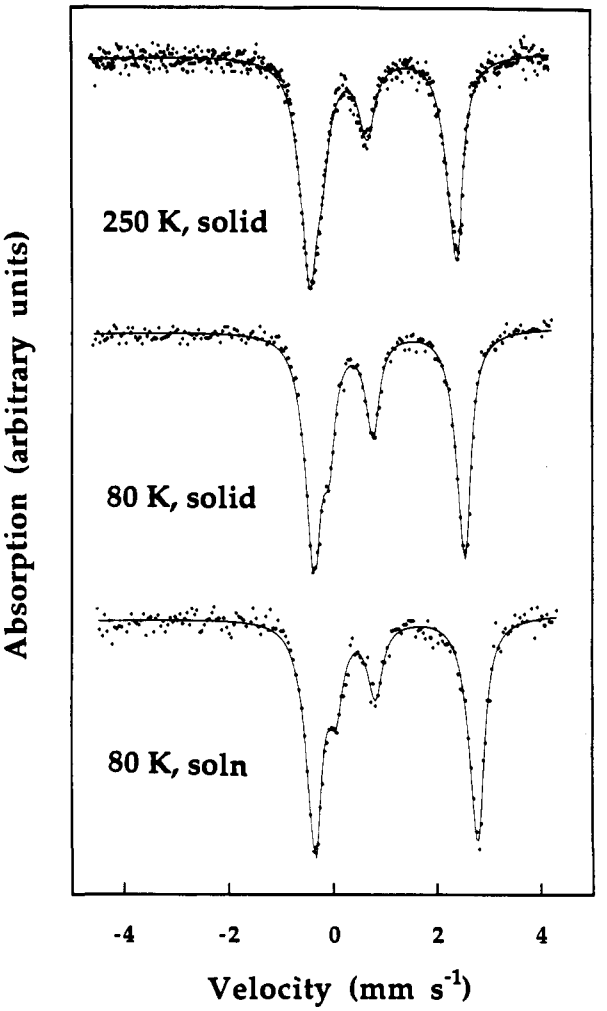

Figure 9. Mössbauer spectra of polycrystalline [Fe$_4$(OMe)$_5$(MeOH)$_3$(OBz)$_4$] (3) at 250 K (top) and 80 K (middle) and at 80 K in a 50% CH_2Cl_2/50% MeOH solution (bottom).

impurity which accounts for less than 5% of the overall resonant area. The slight change in ΔE_Q for the iron(III) component of 3 may be due to differences in hydrogen bonding between the terminal methoxide coordinated to Fe(1) in the crystal lattice versus solution. As expected, the line width at half-height, Γ, for the features increases somewhat for the frozen solution spectra, but the overall resonances remain unchanged when compared to those of the solid samples. These findings provide further evidence for the structural integrity of the cubes in solvent mixtures containing methanol. As found in the ^{1}H NMR spectrum of 2, the symmetry of the iron methoxide core appears to be retained upon dissolution, a conclusion that also applies to the mixed-valent cube 3.

Several of the mixed-valent diiron(II,III) complexes listed in Table VI become valence-detrapped at higher temperatures.[39] The variable-temperature Mössbauer spectra for [Fe$_2$(OAc)$_2$(bimp)]$^{2+}$ and its derivatives have been examined in detail, and the rate of electron transfer between iron centers has been found to be greater than the ^{57}Fe Mössbauer excited-state lifetime in several cases. Complexes [Fe$_2$(OAc)$_2$(HXTA)]$^{2-}$ and [Fe$_2$(salmp)$_2$]$^-$ also begin to undergo fast electron exchange above 100 K.[44] These complexes exist in both the valence-trapped and detrapped forms over a range of temperatures. In contrast, the pyridyl derivative [Fe$_2$(OPr)$_2$(BPMP)]$^{2+}$ remains valence-trapped up to 300 K. Such was also the case for complex 3, as evidenced by the 250 K solid-state spectrum (Figure 9). The specific reason for these different behaviors is uncertain. The mineral vivianite exhibits no electron delocalization at room temperature, nor does complex 5.[23,35]

Low-temperature Mössbauer spectra were measured for all three iron alkoxide cubes. Compound 1 exhibits a single quadrupole doublet down to 4.2 K. A pronounced temperature dependence is observed in its quadrupole splitting parameter, which ranges from 1.48 mm s^{-1} at 280 K to 2.35 mm s^{-1} at 4.2 K (Table VI). Octahedrally coordinated high-spin ferrous ion often has its T_{2g} ground-state orbital degeneracy lifted through axial ligand field distortions and spin–orbit interactions. Thermal population of these low-lying levels gives rise to variations in ΔE_Q with temperature.[37,46]

In contrast to 1, the low-temperature Mössbauer spectra for polycrystalline samples of 2 and 3 exhibit magnetic hyperfine structures in the absence of an applied field. Figures 10 and 11 depict several low-temperature spectra for the two compounds. At 6 K for complex 2, intermediate spin relaxation is realized, and sharp magnetic hyperfine features develop below 4.2 K. From the outer absorption signals for the 1.8 K data, two slightly inequivalent magnetic iron(II) subcomponents, labeled I and II, have been identified, and their spectral parameters are listed in Table VI. Additional broad absorption lines in the central region arise from dynamic spin relaxation phenomena that become the dominant spectral component at slightly elevated temperatures. The transition to a slow-relaxation regime occurs over a rather small temperature range of only ~2 K. Similarly, for complex 3, well-resolved magnetic hyperfine interactions evolve rapidly with decreasing temperatures. Again, from the outer absorption

(46) Greenwood, N. N.; Gibb, T. C. *Mössbauer Spectroscopy*; Chapman & Hall, Ltd.: London, 1971.

Table VI. Selected Mössbauer Spectral Parameters for Polynuclear Iron–Oxygen Complexes[a]

compound	T, K	δ, mm s^{-1}	ΔE_Q, mm s^{-1}	Γ, mm s^{-1}	A, %	H_{hf}, T	ref
Iron(II) Complexes							
1, solid	280	1.14	1.48	0.42	100		*b*
	240	1.16	1.52	0.46	100		
	200	1.19	1.67	0.42	100		
	160	1.21	1.85	0.42	100		
	120	1.22	2.06	0.46	100		
	80	1.24	2.25	0.40	100		
	4.2	1.25	2.35	0.44	100		
2·toluene, solid	80	1.21	2.52	0.30	100		*b*
site I[c]	1.8	1.23	0.38	1.10	34	23.2	
site II		1.23	−0.47	0.80	35	29.8	
2·toluene, solution[d]	80	1.21	2.52	0.40	*e*		*b*
	4.2	1.22	2.54	0.36	100		
$[Fe_2(O_2CH)_4(BIPhMe)_2]$	4.2	1.2	3.30	*f*	*g*		45
		1.26	2.56				
$[Fe_2(OPr)_2(BPMP)]^+$	93	1.20	2.79	0.29	*g*		37
		1.21	2.31	0.39			
Valence-Trapped Iron(II,III) Complexes							
3, solid	250	0.48	0.88	0.38	27		*b*
		1.20	2.86	0.38	73		
	80	0.53	0.89	0.32	29		
		1.28	3.05	0.34	71		
site I[c]	1.8	0.52	0	0.78	22	43.9	
site II, a		1.38	−0.53	0.40	20	26.5	
site II, b		1.38	0.15	0.44	17	25.8	
site II, c		1.38	0.77	0.44	16	24.9	
3, solution[h]	80	0.53	0.77	0.34	25		*b*
		1.31	3.17	0.36	75		
5	20	0.47	0.74	0.38	29		23
		1.28	2.02	0.52	55		
		1.29	3.29	0.34	16		
$[Fe_2(OPr)_2(BPMP)]^{2+}$	55	0.48	0.54	0.30	52		39c
		1.13	2.91	0.29	48		
$[Fe_2(OAc)_2(bimp)]^{2+}$	110	0.51	0.32	*f*	*i*		39d
		1.16	1.69				
$[Fe_2(OAc)_2(L\text{-}Bzim)]^{2+}$	77	0.58	0.40	0.30	*j*		39b
		1.29	2.81	0.28			
$[Fe_2(OAc)_2(HXTA)]^{2-}$	55	0.50	0.37	*f*	*g*		39a
		1.23	2.87				

[a] δ = isomer shift, ΔE_Q = quadrupole splitting, Γ = width at half peak height, A = resonant absorption area normalized to 100% for the total resonant area. For magnetically split spectra, ΔE_Q becomes ϵ, where $\epsilon = (1/4)\Delta E_Q(3\cos^2\theta - 1)$ and θ is the angle between the principal component of the electric field gradient and the direction of the hyperfine field at the site of the nucleus.[46] [b] This work. [c] A broad quadrupole double was introduced to account for the unresolved central absorption area due to intermediate relaxation effects. [d] 90% toluene/10% MeOH. [e] A 5% iron(III) impurity was present in the sample. [f] Not reported. [g] Reported to be of equal intensity. [h] 50% toluene/50% MeOH. [i] Constrained to be of equal intensity. [j] Ratio of iron(III) to iron(II) absorption area is 1.1.

features, iron(III) and iron(II) components, sites I and II, respectively, can be identified. The differential broadening of the outermost absorption lines for the ferrous feature indicates that site II envelops three slightly inequivalent magnetic substructures. These spectral parameters are listed for the 1.8 K spectra in Table VI. The central absorption lines could be reproduced by introducing nonvanishing asymmetry parameters η for the iron(II) site, where η introduces a rhombic distortion to the iron centers.[46] Due to the complexity of the spectrum, however, unique values of η could not be determined. The dynamic relaxation phenomena observed above 4.2 K may also persist and contribute to the low-temperature spectrum.[47]

The origin of the slow-relaxation magnetic behavior in the presence of iron(II) is difficult to establish.[48] Detailed spectral analysis indicates that the magnitude of the hyperfine fields for **2** and **3** remain approximately constant with increasing temperature. The widths of the absorption lines, however, diverge as the transition to a fast-relaxation regime is approached. The absence of variation in H_{hf} with temperature precludes the presence of three-dimensional intermolecular magnetic ordering,[48] and this finding is consistent with magnetization measurements discussed below, for which no discontinuities were found. The temperature dependence of the magnetic hyperfine structure is compatible, however, with a lower dimensional intermolecular interaction.[49]

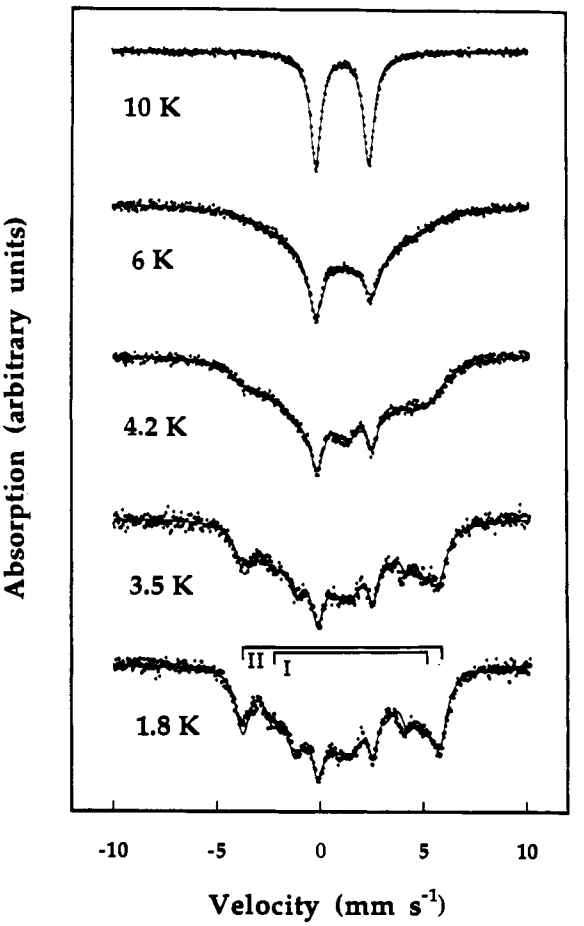

Figure 10. Mössbauer spectra of polycrystalline [Fe(OMe)(MeOH)(DBM)]$_4$·toluene, (**2**)·toluene, at 10, 6, 4.2, 3.5, and 1.8 K. The solid lines are least-squares fits to the data. The outer absorption components of sites I and II are designated for the 1.8 K spectrum.

In order to study this possibility, the frozen solution Mössbauer spectra of **2** and **3** in toluene/MeOH and CH_2Cl_2/MeOH solvent mixtures, respectively, were measured at 4.2 K. The results of these experiments are depicted in Figures 12 and 13 along with the spectra of polycrystalline samples recorded at the same temperature for comparison. For slow paramagnetic relaxation dominated by single-ion anisotropy,[50] magnetic dilution of the cubes should further diminish potential spin relaxation pathways and raise the onset temperature of the magnetic structure in the Mössbauer spectra. The opposite effect was observed for **2** and **3**, however. Fast paramagnetic relaxation with no magnetic hyperfine interactions was observed for frozen solutions of **2**; for **3**, only about 15% of the Mössbauer absorption arose from broad unresolved magnetic subspectra. The frozen solution data are therefore consistent with the notion that the source of the magnetic splitting is not slow paramagnetic relaxation but rather is intermolecular in nature. This interpretation assumes that the cubes are stable in solution, a conclusion supported by the high-temperature Mössbauer, electronic spectral, and ^{1}H NMR measurements.

(47) Van der Woude, F.; Dekker, A. J. *Phys. Status Solidi* **1965**, *9*, 775.
(48) Reiff, W. M. In *Chemical Mössbauer Spectroscopy*; Herber, R. H., Ed.; Plenum Press: New York, 1984; p 65.
(49) Prasanna, T. R. S.; O'Handley, R. C.; Kalongji, G.; Papaefthymiou, G. C. *Phys. Rev. B* **1993**, *47*, 3374 and references therein.
(50) Nicolini, C.; Reiff, W. M. *Inorg. Chem.* **1980**, *19*, 2676.

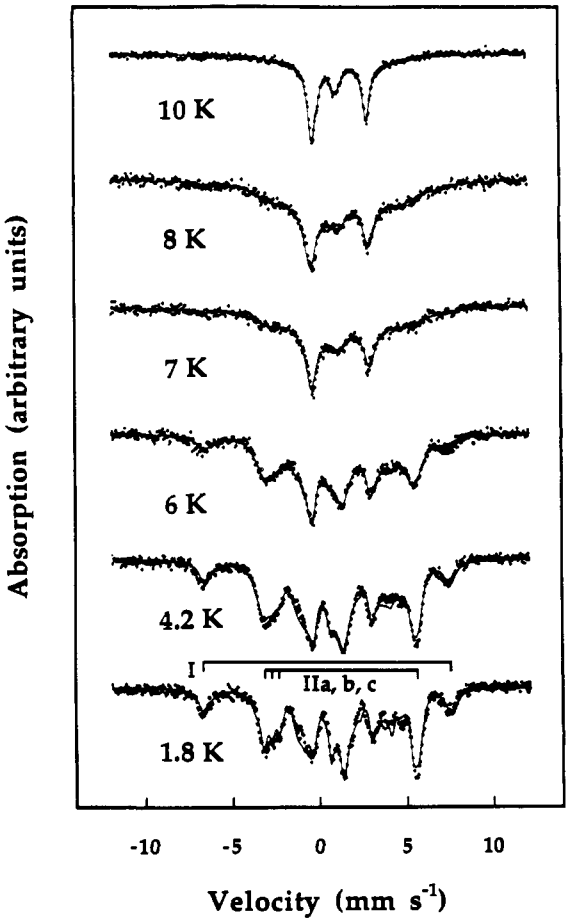

Figure 11. Mössbauer spectra of polycrystalline $[Fe_4(OMe)_5(MeOH)_3(OBz)_4]$ (3) at 10, 8, 7, 6, 4.2, and 1.8 K. The solid lines are least-squares fits to the data. For the 1.8 K spectrum, the outer absorption components for sites I and II (a,b,c) are marked.

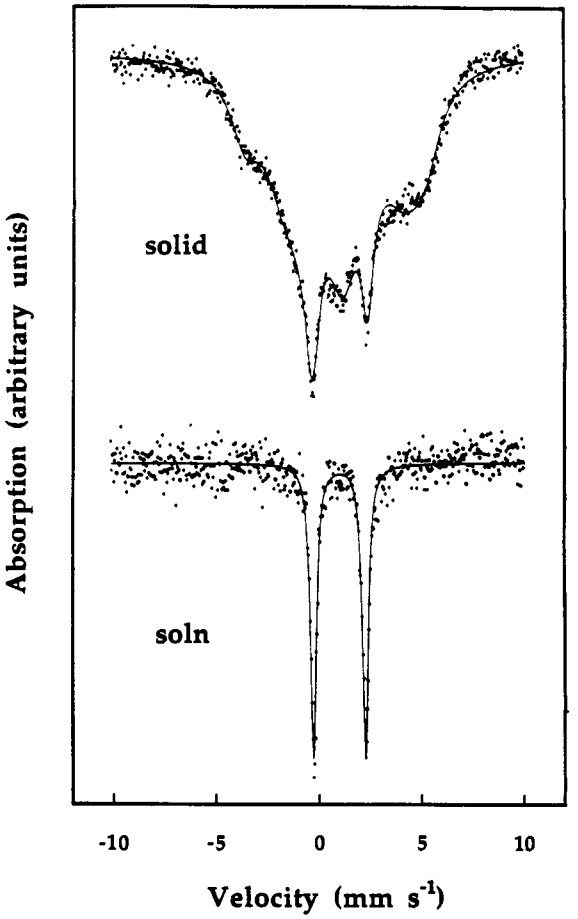

Figure 12. Solid (top) and solution (bottom) Mössbauer spectra for [Fe(OMe)(MeOH)(DBM)]4·toluene, (2)·toluene, at 4.2 K. The best-fit lines for the two spectra are drawn.

Magnetic hyperfine interactions in the absence of an applied field have been observed for other iron(II) and iron(II,III) systems, including $[Fe_2(OPr)_2(BPMP)]^{2+}$ and $[Fe_2(OAc)_2(HXTA)]^{2-}$, and have been explicitly described and fit for $[Fe(acac)_2]_2$ and $[Fe_2(salmp)_2]^-$.[39,44,50] For $[Fe_2(salmp)_2]^-$, a large anisotropy accounted for the magnetic hyperfine interaction and slow relaxation was also observed in solution.[44] For complexes **2** and **3**, the most probable explanation for the low-temperature Mössbauer behavior is the presence of lower dimensional pathways for magnetic communication among molecules in the crystal lattice.

Magnetic Properties. The magnetic properties of the two iron cubes **1** and **3** were investigated in both variable-temperature and variable-field experiments. The magnetism of the manganese cube **4** will be described in a future publication. The magnetic behavior of **2** was difficult to interpret, and we do not present it here. The magnetism of transition-metal ions with $^{(2S+1)}T_{1,2g}$ ground states, including Fe(II), is typically complicated by factors such as large anisotropy, zero-field splitting, and orbital contributions to the magnetization. For example, the magnetization of the ferrous ion in $(NH_4)_2Fe(SO_4)_2{\cdot}6H_2O$ is canted away from the applied field by approximately 40% in fields up to 5 T.[51] The orientation of the canting was not easily reconciled with the molecular geometry. Even with single-crystal magnetic data it is often difficult to interpret definitively the magnetic properties of mononuclear ferrous systems.[52] Exchange coupling among ironatoms of the $\{Fe_4(OMe)_4\}^{n+}$ core further complicates the analysis. For these reasons, the parameters derived from the magnetic studies of **1** and **3** reported below are considered effective values, to be used only when making comparisons among these structurally related complexes.

The temperature dependence of χT for the tetrairon(II) and mixed-valent iron(II,III) cubes is depicted in Figure 14. For compound **1**, χT increases from 16.5 emu mol^{-1} K at 300 K to a maximum of 31 emu mol^{-1} K at 5 K, below which it decreases slightly. The theoretical room-temperature χT value for four uncoupled iron(II) ions with $g = 2.25$ is 15.2 emu mol^{-1} K.[17] The smooth increase in χT over the entire temperature range is indicative of ferromagnetic coupling among the iron centers, and the decrease below 5 K is most likely a result of zero-field splitting. The increase in χT with decreasing temperature was not due to orientation of the crystallites in an applied magnetic field as a result of single-ion zero-field splitting,[53] since care was taken to restrain the sample from reorienting during the measurement. The mixed-valent $\{Fe_4(OMe)_4\}^{5+}$ cube **3** has dramatically different magnetic properties. The χT value decreases from 15 emu mol^{-1} K at room temperature to 2.36 at 3.5 K, a behavior characteristic of antiferromagnetic, not ferromagnetic, coupling among the iron centers. By using g values of 2.25 for the iron(II) and 2.0 for the iron(III) ions, the spin-only χT value for **3** was calculated to be 15.8 emu mol^{-1} K, consistent with the room-temperature measurement.

The temperature dependence of χT for **1** was fit by using a single exchange constant for the six Fe···Fe interactions, which effectively assumes T_d symmetry. Fits using a model with two independent exchange interactions corresponding to the molecular

(51) Figgis, B. N.; Forsyth, J. B.; Kucharski, E. S.; Reynolds, P. A.; Tasset, F. *Proc. R. Soc. London* **1990**, *428*, A113.

(52) (a) Gerloch, M. *Magnetism and Ligand Field Analysis*; Cambridge University Press: Cambridge, U.K., 1983. (b) Gerloch, M.; Quested, P. N. *J. Chem. Soc. A* **1971**, 2307.

(53) Charron, F. F., Jr.; Reiff, W. M. *Inorg. Chem.* **1986**, *25*, 2786.

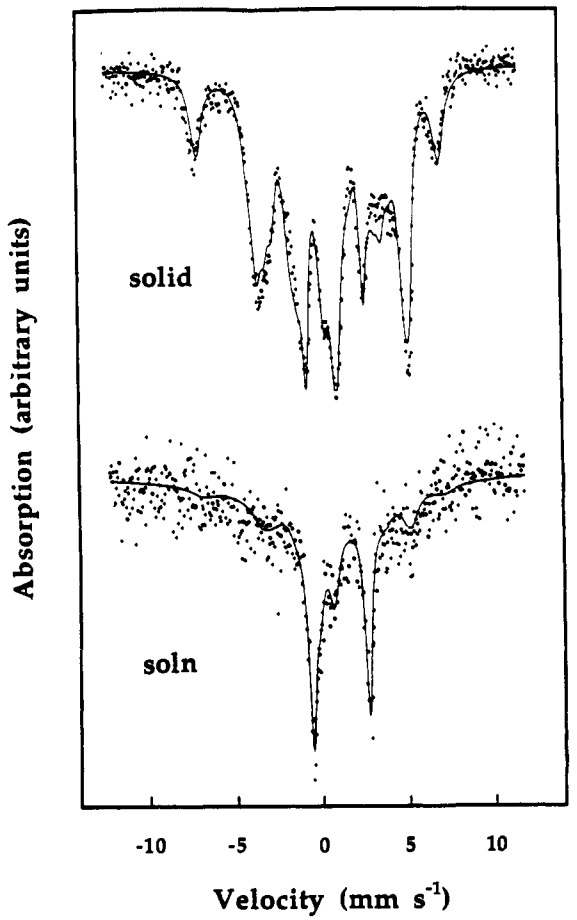

Figure 13. Solid (top) and solution (bottom) Mössbauer spectra for $[Fe_4(OMe)_5(MeOH)_3(OBz)_4]$ (3) at 4.2 K. In the fit of the solution spectra, magnetic subspectra with parameters similar to those observed for the solid sample were superimposed within the broad background absorption.

S_4 symmetry observed in the structural study failed to give a unique set of parameters; the two J values were strongly correlated. In the limit of Heisenberg-like exchange and with the Hamiltonian $J\sum_{i,j}\mathbf{S}_i\cdot\mathbf{S}_j$ where $j > i$, the energies of the spin states determined according to the Kambe vector coupling model are given by eq 3, where $S_i = 2$ for iron(II) and S_T can range from 0 to 8.[54] A

$$E(S_T) = \frac{J}{2}[S_T(S_T + 1)] \quad (3)$$

total of 85 spin levels giving rise to 625 magnetic components were present in the spin manifold. Only data above 30 K were included in the fit to minimize the influence of zero-field splitting. A small, ferromagnetic J value of -1.88 cm^{-1} was determined, with $g = 2.29$. The fit is shown as a solid line in Figure 14. Cubane complexes having the $\{Ni_4(OMe)_4\}^{4+}$ core are also ferromagnetically coupled, with exchange coupling constants of several wavenumbers.[20]

Two different exchange constants were used to evaluate the magnetic properties of **3**, one for the iron(II)–iron(II), J_1, and one for the iron(II)–iron(III), J_2, interactions. The Hamiltonian for this model is given in eq 4,[55] where $S_1 = S_2 = S_3 = 2$ for

$$H = J_1(\mathbf{S}_1\cdot\mathbf{S}_2 + \mathbf{S}_1\cdot\mathbf{S}_3 + \mathbf{S}_2\cdot\mathbf{S}_3) + J_2(\mathbf{S}_A\cdot\mathbf{S}_4) \quad (4)$$

iron(II), $S_4 = {}^5/_2$ for iron(III), and $\mathbf{S}_A = \mathbf{S}_1 + \mathbf{S}_2 + \mathbf{S}_3$. The resulting energy levels are given in eq 5, where $\mathbf{S}_T = \mathbf{S}_A + \mathbf{S}_4$.

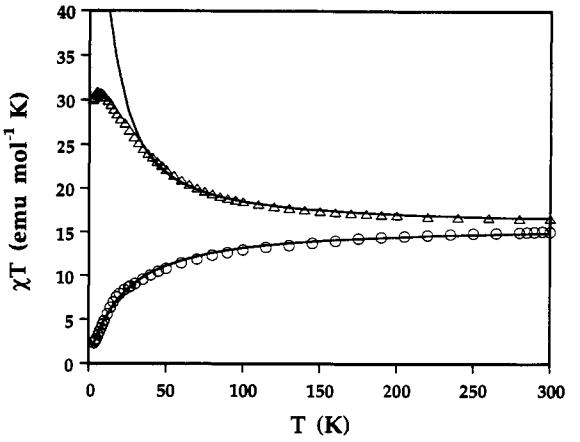

Figure 14. Plot of χT versus temperature for $[Fe(OMe)(MeOH)(DPM)]_4$ (1) (△) and $[Fe_4(OMe)_5(MeOH)_3(OBz)_4]$ (3) (○). The solid lines are the calculated χT values for the two iron alkoxide complexes as described in the text.

$$E(S_A,S_T) = \frac{J_1}{2}[S_A(S_A + 1)] + \frac{J_2}{2}[S_T(S_T + 1) - S_A(S_A + 1)] \quad (5)$$

There are 95 spin states for this complex, with 750 magnetic subcomponents. From a least-squares fit of the data over the entire temperature range, a g value of 2.18 and J_1 and J_2 values of 2.60 and 1.63 cm^{-1}, respectively, were determined. The composite g value found, 2.18, is approximately equal to the average of $g = 2.25$ for the three iron(II) ions and $g = 2.00$ for the single iron(III) site.

Variable-field measurements from 0 to 20 T at 1.2 and 0.6 K for **1** and **3**, respectively, were made to examine further their magnetic properties. The reduced magnetization versus field is plotted in Figure 15. For **1**, $M/N\mu_B$ increases rapidly at low fields and gradually saturates, reaching a maximum value of 15.7 μ_B at 19.7 T. The ferromagnetic coupling of the ferrous ions described above gives a $S_T = 8$ ground state, which has a theoretical saturation moment of 18 μ_B for $g = 2.25$.[17] The depressed value found for **1** results from zero-field splitting in the $S_T = 8$ spin manifold. The first excited state has a spin of 7 and, for a J value of 1.89 cm^{-1}, lies 15 cm^{-1} above the $S_T = 8$ ground state. The magnetization for **3** does not saturate, and is still increasing even at 20 T. According to the calculated exchange interactions, seven spin states with S_T from ${}^1/_2$ to ${}^5/_2$ are grouped within 10 cm^{-1} of the ground state. Moreover, the first excited state, which has $S_T = {}^3/_2$, lies only 0.51 cm^{-1} above the $S_T = {}^1/_2$ ground state. Anisotropy effects are expected to influence the magnetization as well, so for these reasons, the data for **3** were not examined quantitatively. The behavior appears to be consistent with the antiferromagnetic coupling determined from the variable-temperature measurements.

The reduced saturation magnetization for **1** was evaluated to determine the contribution from zero-field splitting and to verify the postulated $S_T = 8$ ground state. The powder magnetization was calculated from known expressions,[56] and the 1.2 K data were reproduced with $D = 3$ cm^{-1}, $E/D = 0.075$, and $g = 2.2$, as shown in Figure 15. This result confirms the identity of the ground spin state and is consistent with the presence of appreciable zero-field splitting. Nickel(II) cubes with methoxide bridges also exhibit a significant anisotropy in their magnetism.[57]

The ferromagnetic coupling found for **1** is unusual in iron–oxygen chemistry, and few polyiron complexes have a ground state with the maximum possible spin.[9] Some iron(II) and mixed-

(54) Sinn, E. *Coord. Chem. Rev.* **1970**, *5*, 313.
(55) (a) Noodleman, L. *Inorg. Chem.* **1991**, *30*, 246. (b) Belinskii, M. *Chem. Phys.* **1993**, *172*, 189 and 213.
(56) (a) Gerloch, M.; McMeeking, R. F. *J. Chem. Soc. Dalton Trans.* **1975**, 2443. (b) Blake, A. B. *J. Chem. Soc. Dalton Trans.* **1981**, 1041.
(57) Barnes, J. A.; Hatfield, W. E. *Inorg. Chem.* **1971**, *10*, 2355.

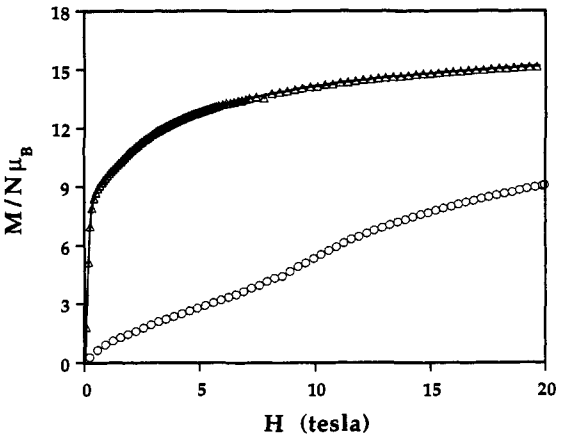

Figure 15. Plot of $M/N\mu_B$ versus field for [Fe(OMe)(MeOH)(DPM)]$_4$ (**1**) (Δ) and [Fe$_4$(OMe)$_5$(MeOH)$_3$(OBz)$_4$] (**3**) (O) at T = 1.2 K. The solid line fit for **1** is the calculated magnetization for an S_T = 8 spin state with D = 3 cm^{-1}; E/D = 0.075, and g = 2.2.

valent iron(II,III) exceptions have been described.[31,58] Ferromagnetic behavior appears to be characteristic of the {M$_4$(OMe)$_4$}$^{4+}$ core, at least for the even spin systems Fe(II) and Ni(II). The cubane complex **3**, in contrast to **1**, is antiferromagnetically coupled. This difference may be a consequence of the bridging benzoate ligands, which provide an additional pathway for electronic exchange and distort the {Fe$_4$(OMe)$_4$}$^{n+}$ core. The MeO–Fe–OMe and Fe–OMe–Fe angles for **1** have very consistent values, whereas these same parameters in **3** are spread over a greater range. These variations may be sufficient to alter the observed magnetic behavior. Such subtle effects have been studied in detail for dinuclear metal complexes,[59] and several {Ni$_4$(OR)$_4$}$^{4+}$ cubane species have both antiferromagnetic and ferromagnetic exchange interactions,[21] in contrast to that observed for the {Ni$_4$(OMe)$_4$}$^{4+}$ cubes.[20,57] The higher oxidation state for cube **3** as compared to **1** may also be responsible for the different magnetic behavior. The absolute values of the coupling constants calculated for both **1** and **3**, however, are quite similar. The orbital pathway for exchange interactions in both cubes involves predominantly the bridging methoxide ligands, and the resulting exchange constants are relatively weak. Triply-bridging methoxide ligands are therefore poor mediators of exchange coupling for iron(II) and iron(III).

(58) Rardin, R. L.; Poganiuch, P.; Bino, A.; Goldberg, D. P.; Tolman, W. B.; Liu, S.; Lippard, S. J. *J. Am. Chem. Soc.* **1992**, *114*, 5240. Recent work in our laboratory (D. P. Goldberg, unpublished results) has shown the low temperature χT for the triiron(II) compound described in this paper to be consistent with an S_T = 6 ground state and no intercluster interaction as originally suggested. A detailed report is forthcoming.

(59) Kahn, O. *Angew. Chem., Int. Ed. Engl.* **1985**, *24*, 834.

Conclusions

The four {M$_4$(OR)$_4$}$^{n+}$ cubes described here are valuable additions to the coordination chemistry of lower valent iron and manganese. With the characterization of **1–4**, the cubane geometry known for other metal–ligand systems can now be considered a feature of iron and manganese alkoxide chemistry as well. The solid-state properties of these cubes have been determined, and furthermore, they appear to be stable in solutions which contain the appropriate alcohol. The isolation of both the {Fe$_4$(OMe)$_4$}$^{4+}$ and {Fe$_4$(OMe)$_4$}$^{5+}$ cores demonstrates that this molecular architecture can support mixed oxidation states. Future work for both iron and manganese will include synthetic efforts to access this molecular architecture in higher oxidation states.

Acknowledgment. This work was supported by a grant from the National Science Foundation. K.L.T. is grateful to the National Science Foundation for a Graduate Research Fellowship, A.C. acknowledges the Consiglio Nazionale delle Richerche Comitato Nazionale Scienze Chimiche for support, and L.E.P. thanks the National Cancer Institute for a postdoctoral fellowship. We thank Dr. A. Masschelein for fitting the electronic spectra of **3**, D. Western and J. Owens of the M.I.T. Spectrometry Laboratory for assisting with the ^{1}H NMR measurements of **1** and **2**, and E. J. McNiff, Jr., of the Francis Bitter National Magnet Laboratory for carrying out the magnetization measurements of **1** and **3**.

Supplementary Material Available: Tables of atomic positional parameters and equivalent isotropic thermal parameters, anisotropic temperature factors, and selected bond distances and angles for **1–4** and ^{1}H NMR spectra of **1** and **2** (38 pages). This material is contained in many libraries on microfiche, immediately follows this article in the microfilm version of the journal, and can be ordered from the ACS; see any current masthead page for ordering information.